

M2-Internship Report: Eye Kalman Project

Pierre-Antoine Senger

Supervised by:

Christophe Prud'homme
Thomas Saigre
Marcela Szopos

University of Strasbourg
University of Strasbourg
Paris Cité University

Date: August 25, 2025

Contents

1	Introduction	3
1.1	Context	3
1.2	Laser Applications in Ophthalmology for Disease Management	5
1.3	Laser-Tissue Interaction	6
1.4	Main Objectives	7
1.5	Software and Libraries	8
1.6	Outline	8
2	State of the Art	8
2.1	Historical Studies on Ocular Thermal Modeling	9
2.2	Recent Advances in Laser-Ocular Thermal Modeling	9
2.3	Pulsed Laser Interactions with Ocular Tissue	10
2.4	Parameter Estimation in Biological Tissues	10
2.5	Summary and Future Directions	10
3	Mathematical Modeling	11
3.1	The Pennes Bioheat Equation	12
3.2	The Radiative Transfer Equation (RTE)	13
3.3	The Diffusion Approximation	14
3.4	Pennes and Diffusion Approximation Coupling	16
3.5	Physical Parameters	16
4	Mathematical and Computational Framework	19
4.1	The Monte Carlo Method (RTE-MC)	20
4.1.1	Photon Propagation	20
4.1.2	Photon Scattering	21
4.1.3	Photon Absorption	23

4.1.4	Interface Handling	24
4.1.5	Russian Roulette	26
4.1.6	RTE-MC Summary	26
4.2	Pennes Bioheat and RTE-MC Coupling	27
4.3	The Variational Formulation	27
4.3.1	The Variational Formulation of the Heat Equation	28
4.3.2	The Variational Formulation of the DA	29
4.4	Finite Element Discretization	30
4.5	Time Scheme	31
4.6	Heat Equation Discretization	31
4.7	Diffusion Approximation Equation Discretization	31
5	Simulations	33
5.1	Eye Geometry	33
5.2	Solver Settings	34
6	Numerical Results	35
7	Toward solving the Inverse Problem	39
7.1	Kalman-type Filtering Algorithms	40
7.2	Classical Kalman Filter	40
7.3	Ensemble Kalman Filter (EnKF)	41
8	Conclusion	42
9	Prospects	43
Appendix A: Approximation Error Metrics		44
A	References	46

1 Introduction

This internship took place at Cemosis, the Center for Modeling and Simulation in Strasbourg, in collaboration with the University of Strasbourg. It is part of a larger effort to develop a digital twin of the human eye, combining advanced mathematical modeling, numerical simulation, and data assimilation techniques. Within this broader context, the present work focuses on understanding and simulating the effect of heat on the human eye during laser treatments. The results obtained during this internship provide a first step toward integrating optical and thermal processes in a comprehensive framework for simulating and managing ophthalmological applications.

1.1 Context

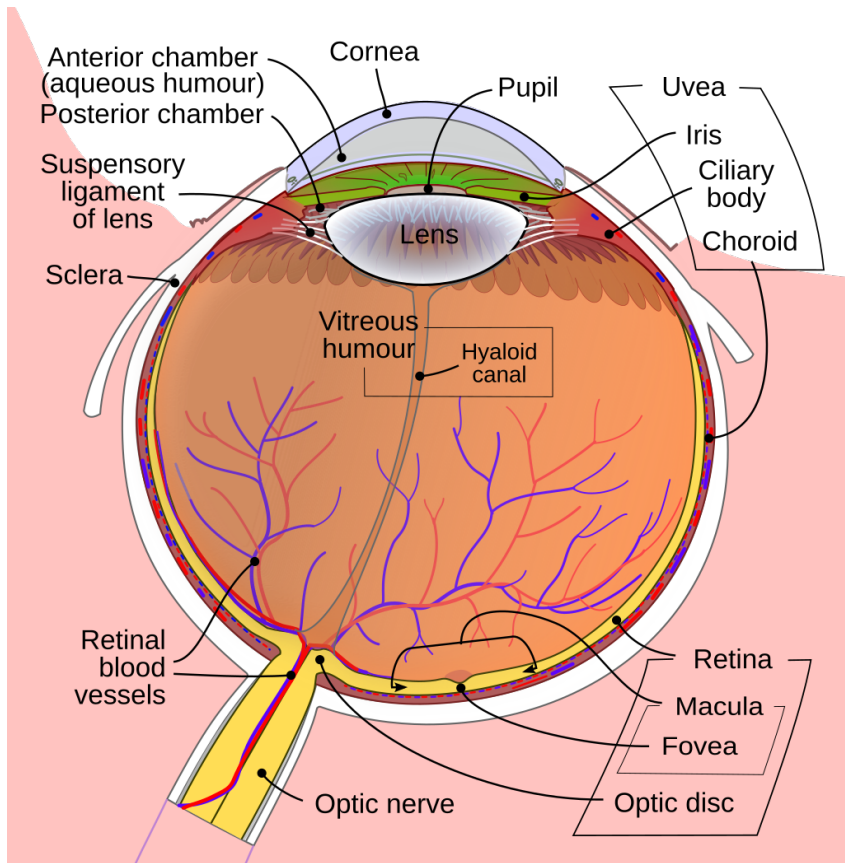


Figure 1: Eye model (Wikipedia).

The human eye, depicted in Figure 1, is considered the second most complex organ after the brain. It is composed of various tissues and fluids that work together to enable vision. The eye can be divided into two main parts:

- **The anterior segment** (from the Latin *ante* before), which includes the cornea, iris, ciliary body, and lens.

- **The posterior segment** (from the Latin *post* after), which includes the vitreous humor, retina, choroid, and optic nerve.

Each of these structures plays a crucial role in the visual process. The **cornea** is the first structure that light encounters when entering the eye and is responsible for refracting light onto the **lens**, which further focuses the light onto the **retina**. In the retina, light is converted into electrical signals that are transmitted to the brain via the **optic nerve**.

The **ciliary body** adjusts the shape of the lens to allow focus on objects at different distances. The **iris** regulates the amount of light entering the eye by controlling the size of the **pupil**.

The **aqueous humor** is a clear fluid that nourishes the cornea and lens while helping maintain intraocular pressure. The **vitreous humor** is a gel-like substance that helps maintain the eye's shape and provides support to the retina.

The **retina** consists of **nine layers** of neural cells (Figure 2), including photoreceptors, bipolar cells, and ganglion cells. It also contains a **retinal pigment epithelium (RPE)** layer, which absorbs excess light and provides nutrients to the photoreceptors.

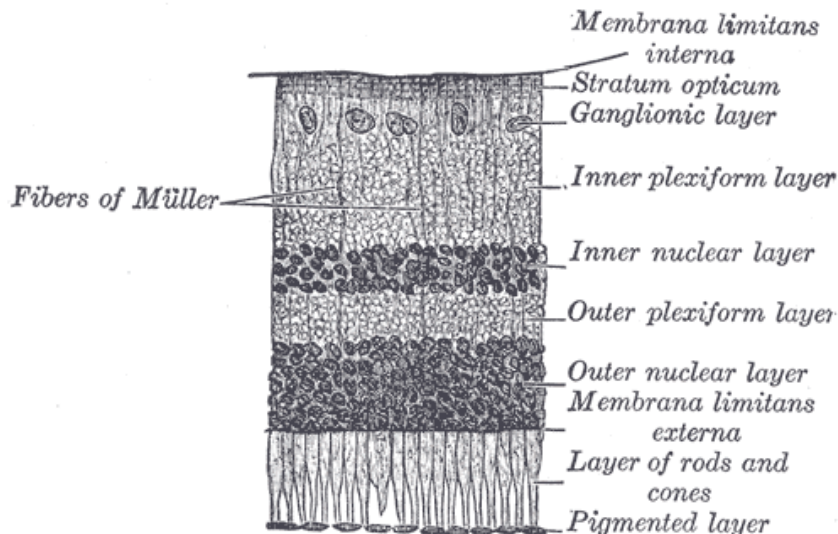


Figure 2: Section of retina (Wikipedia).

The **choroid** is a layer of blood vessels that supplies oxygen and nutrients to the retina. The **optic nerve** is a bundle of nerve fibers that transmits electrical signals from the retina to the brain.

The **sclera** is the white outer layer of the eye that provides protection and structural support. The **conjunctiva** is a thin, transparent membrane covering the sclera and the inside of the eyelids.

The **lacrimal gland** produces tears that keep the eye moist and help protect it from infection. The **extraocular muscles** control eye movement, while the **eyelids** protect the eye and distribute tears across its surface. The **tear film** is a thin layer of fluid

covering the eye's surface, maintaining a smooth optical surface and helping to cool the eye.

1.2 Laser Applications in Ophthalmology for Disease Management

Laser systems, classified as either continuous wave (CW) or pulsed lasers, are commonly used in the treatment of various eye conditions. A wide range of ocular pathologies can lead to vision disorders, many of which can be effectively managed with laser therapy. Depending on the condition, lasers may be used to **reshape tissue, induce coagulation, or remove abnormal tissue**, making them valuable tools in procedures such as refractive surgery, glaucoma management, retinal vessel coagulation, and cataract removal, among others.

Given the eye's complexity and sensitivity, understanding how **laser light interacts with ocular tissues** is essential to ensure safe and effective treatments. Moreover, the **optical properties of biological tissues can vary between individuals and change with heating**, making it difficult to accurately predict and optimize treatment outcomes. The lack of direct measurements in some cases adds another layer of complexity to the process.

This variability highlights the importance of **mathematical models and simulations** in ophthalmology. These tools help researchers and clinicians understand and refine laser treatment parameters for improved precision and safety.

Tables 1 and 2 summarize some of the laser treatments commonly used for the anterior and posterior segments of the eye while Table 3 provides details on laser surgery types and key parameters.

Table 1: Laser treatments for the anterior segment of the eye.

Structure	Pathology	Laser Treatment	Reference
Cornea	Refractive errors	LASIK, SMILE, PRK	[Oph23]
	Keratoconus	Corneal cross-linking	[Med22]
Iris	Pigment dispersion syndrome	Selective laser trabeculoplasty (SLT)	[Tim22]
Pupil	Traumatic mydriasis	Laser iridoplasty / pupilloplasty	[Eye21]
Ciliary Body	Ciliary block glaucoma	Laser cyclophotocoagulation	[Eye21]
Trabecular Meshwork	Open/angle-closure glaucoma	SLT, Argon laser trabeculoplasty (ALT)	[Tim22]
Lens	Cataracts	Femtosecond laser-assisted surgery (FLACS)	[Pub14]
	Presbyopia	Laser scleral microporation	[Pub14]

Table 2: Laser Treatments for the Posterior Segment of the Eye.

Structure	Pathology	Laser Treatment	Reference
Neural Retina	Diabetic retinopathy	Panretinal photocoagulation (PRP)	[Tod17]
	Retinal detachment	Laser photocoagulation	[Nor22]
	Age-related macular degeneration (AMD)	Photodynamic therapy (PDT)	[Oph21]
RPE	AMD (RPE atrophy, drusen, CNV)	PDT, Laser photocoagulation	[Oph21]
	RPE-related detachment	Laser photocoagulation	[Oph21]

Table 3: Laser Surgery Types with Key Parameters.

Laser Surgery	Wavelength (nm)	Pulse Duration	Target Tissue	Pathology / Treatment	Reference
Transpupillary Thermotherapy (TTT)	810	60 s	Bulk eye (several mm)	Choroidal melanoma, Isolated choroidal hemangioma, Retinoblastoma	[Eye21]
Panretinal Photo-coagulation (PRP)	577 / 532	50 – 200 ms	Retina or entire fundus (< 1 mm)	Diabetic retinopathy, Retinal neovascularization, Choroidal hemangioma, Retinal hemangioma	[Tod17]
Subthreshold Diode Micropulse (SDM)	532 / 810	100 µs	Retinal pigment epithelium (RPE, 10 µm thick)	Diabetic macular edema, Branch retinal vein occlusion, Central serous chorioretinopathy, Inherited retinopathies	[Tod17]
Selective Retina Therapy (SRT)	532	1 – 10 ns	Melanin particles in RPE (2 µm)	Diabetic macular edema, Age-related macular degeneration, Central serous chorioretinopathy	[Tod17]

1.3 Laser-Tissue Interaction

Lasers concentrate light into a tightly focused beam. When this beam interacts with tissue, the light energy can be **reflected, scattered, absorbed, or transmitted**, as illustrated in Figure 3. When absorption occurs, part of the light energy is converted into heat, which can lead to **thermal damage** in the tissue.

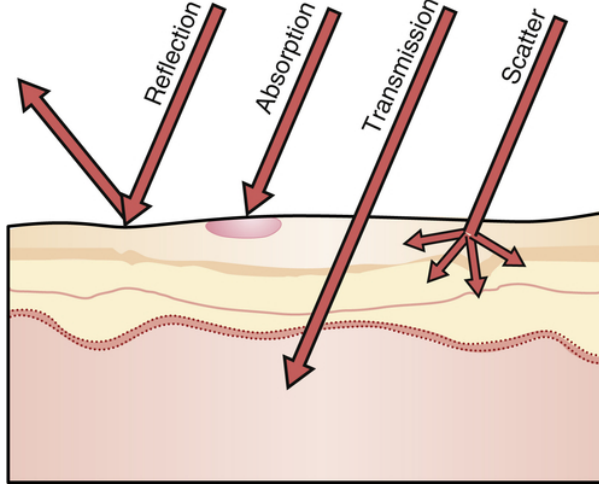


Figure 3: Laser tissue interactions [Blo19].

The amount of heat generated depends on the **laser parameters** (pulse duration, power, wavelength, beam waist) and the **tissue's optical properties**, such as its **absorption and scattering coefficients**, which vary between different tissues. Notably, tissues exhibit different absorption and scattering coefficients depending on the **wavelength of light**, influencing how laser energy interacts with biological structures.

To minimize damage to nearby tissues micropulse lasers are often used, they work by delivering short pulses of light followed by a resting period. This allows the tissue to cool down between pulses, reducing the risk of thermal damage. When it comes to cutting and shaping tissues the **Femtosecond lasers** are now widely used in ophthalmology. These lasers deliver ultra-short pulses of light that ionize the target tissue, creating a plasma that can ablate the tissue with high precision, minimal collateral damage, and reduced thermal effects [Paj+21]. When thermal damage is desired, for example to coagulate tissues in the case of diabetic retinopathy, **Yellow (577 nm)** were found to be preferable to **Green (532 nm)** lasers [Afl+20a].

1.4 Main Objectives

The first step involves creating a **geometric model** of the eye using preprocessing tools such as Gmsh [GR24] or Salome [RBG17]. This model will be discretized into a mesh, which will be used to **simulate** the heat distribution in the eye tissues.

For simplicity, we will initially assume that the **absorption** and **scattering** coefficients are **known** and **constant**. Using this mesh model, we will solve the Pennes Bioheat equation coupled with the radiative transfer equation (RTE) to simulate the temperature in the eye. The simulation will be performed using the finite element method (FEM) [Wik24b], implemented in Feel++ [Chr+24].

Once we have a solid understanding of the direct problem, we will transition to the **inverse problem**, which involves estimating the absorption and scattering coefficients of eye tissues based on observed temperature distributions. In the context of eye surgery,

temperature data can be captured using an **infrared camera**. To solve this inverse problem, we will employ the **Ensemble Kalman Filter** (EnKF) [Wik24a] [AF22], specifically tailored for parameter estimation.

1.5 Software and Libraries

To create the eye model and mesh it we will use Gmsh [GR24], a powerful 3D finite element mesh generator with a built-in CAD engine and post-processor, and Salome [RBG17], an open-source software that provides a generic platform for pre- and post-processing for numerical simulation.

As for our simulations, our primary tool will be Feel++ [Chr+24], a robust and efficient open-source C++ library designed for solving partial differential equations using the finite element method [Wik24b].

1.6 Outline

The report is structured as follows: Chapter 1 introduces the scientific and practical context of this work, the problem formulation, and the motivations for addressing it. Chapter 2 reviews the state of the art, covering both theoretical and computational approaches that are relevant to our study, and highlights the gaps that motivate our contribution. Chapter 3 details the mathematical modeling of the problem, including the governing equations, assumptions, and physical parameters. In Chapter 4, we present the computational framework and numerical methods employed to solve the problem. Chapter 5 describes the numerical implementation and simulation setup, with particular emphasis on the computational framework and parameter choices. Chapter 6 discusses the obtained results. Chapter 7 gives an overview of the inverse problem formulation for future work. Finally, Chapter 8 summarizes the key findings of this work, while Chapter 9 outlines possible extensions and future research directions. The appendices collect additional derivations and technical details, and the bibliography provides references to the sources used throughout the report.

2 State of the Art

Understanding the thermal response of the human eye to laser radiation has been an active research topic for several decades. Early studies primarily focused on **finite element modeling (FEM)** of temperature distribution in ocular tissues, while more recent studies incorporate **complex bioheat transfer models, multiple wavelengths, and pulsed laser interactions**. In this chapter, we review key contributions to the field, categorized into historical models, recent advancements, and studies on pulsed laser interactions.

2.1 Historical Studies on Ocular Thermal Modeling

Early research on **thermal modeling of the eye** primarily employed **finite element methods (FEM)** and aimed to understand temperature distribution under normal conditions or exposure to external heat sources.

- **A. F. Emery et al. (1975)** [Kra+75]: One of the first studies using **FEM** to simulate temperature distribution in a **2D rabbit eye** exposed to microwaves.
- **J. J. W. Lagendijk (1982)** [J J82]: Developed a **thermal conduction model** to study heat transfer in **human and rabbit eyes** during hyperthermic treatment. Introduced both **steady-state** and **transient** simulations.
- **J. A. Scott (1988)** [Sco88a]: Applied the **bioheat transfer equation** to model heat transport in the human eye. Focused on **temperature distribution in an unexposed eye**.
- **Ng et al. (2008)** [NOR08]: Conducted a comparative study between **2D and 3D human eye models**. Simulated steady-state conditions but **neglected blood perfusion**.

2.2 Recent Advances in Laser-Ocular Thermal Modeling

More recent studies have incorporated **laser energy absorption models**, **3D simulations**, and **refined bioheat transfer models** to analyze the interaction of laser radiation with the human eye.

- **Cvetković et al. (2008)** [CPP08]: Introduced a **3D FEM** model incorporating the **Pennes bioheat equation** and a laser absorption model based on the **irradiance at the retina I_r** .
- **Narasimhan and Jha (2011)** [NJ12]: Simulated **multi-spot laser irradiation** in the **fundus of the eye** using FEM.
- **Mirnezami et al. (2013)** [MRA13]: Extended the work of Cvetković by considering **multiple laser wavelengths**.
- **Heussner et al. (2014)** [Heu+14]: Developed a more **detailed computational model** incorporating **vectorial blood flow** in the **choroid** to improve temperature and damage predictions.
- **Joukar et al. (2015)** [AEH15]: Conducted a **comparative study** on the thermal effects of three different lasers: **Nd:YAP, Nd:YAG, and ArF**.
- **Sahar Rahbar (2018)** [RS18]: Modeled **linear thermal effects** of **ArF (193 nm) and Ho:YAG (2090 nm) lasers** on the anterior eye layers.

- **Aflalo et al. (2020)** [Afl+20a]: Investigated **optimal laser wavelength** for **diabetic retinopathy**. Used a **layered Monte Carlo (MCML)** model for detailed light propagation and a **full-eye FEM model**.
- **Truong et al. (2022)** [TLW22]: Simulated heat transfer in **retinal tissues** and investigated the effects of different laser beam intensity profile ('**top-hat**', **Gaussian** and '**donut**' modes) on temperature distribution.

2.3 Pulsed Laser Interactions with Ocular Tissue

A specialized area of research focuses on **pulsed laser interactions** and their thermal effects on the human eye, particularly in **retinal photocoagulation**.

- **Semenyuk (2017)** [Sem17]: Developed an analytical approach for **multi-pulse laser beam interaction** with **retinal tissue**. Studied Gaussian uniform lasers at **514, 532, and 577 nm**.
- **Zhao et al. (2023)** [Zha+23]: Introduced a **coupled bioheat transfer model** for **whole-eye simulation** in **retinal laser surgery**. Considered a **fundus modeled as a porous tissue matrix** and simulated a **single-spot laser interaction**.

2.4 Parameter Estimation in Biological Tissues

Among the many interesting contributions in this area, we mention here those that are most closely related to our work.

- **Arnold et al. (2014)** [ACS14]: Introduces an adaptation of the ensemble Kalman filter (EnKF) for deterministic stiff systems, allowing parameter and state estimation using indirect, noisy observations. The method incorporates spatial priors and interprets numerical errors as stochastic drift. Demonstrated on metabolic models, it enables parallel computation and improved stability in high-dimensional, ill-posed problems.
- **Arnold and Fichera (2022)** [AF22]: Proposes a computational framework using EnKF to estimate the absorption and scattering coefficients of laser-irradiated tissue, based on thermal response observations. The method can track time-varying optical properties and is compatible with clinical setups using simple thermal sensors. It also estimates additional thermal parameters like heat capacity and conductivity through simulated studies.

2.5 Summary and Future Directions

The evolution of laser-ocular thermal modeling has transitioned from **simplified 2D FEM models** to **detailed 3D simulations incorporating bioheat equations, blood**

perfusion, and multiple laser wavelengths. However, challenges remain, particularly in:

- **Personalized modeling:** Accounting for **inter-patient variability** in tissue optical and thermal properties.
- **Dynamic tissue response:** Including **real-time changes** in perfusion and heat dissipation.
- **Pulsed laser optimization:** Refining **energy deposition models** for **retinal photocoagulation** and laser surgery.

Ongoing research continues to refine these models, leveraging **machine learning**, **Monte Carlo methods**, and **patient-specific simulations** to enhance precision and safety in ophthalmic laser treatments [Mir+21; Kle+21].

3 Mathematical Modeling

In this chapter we introduce the mathematical models that will be used to simulate the heat and light distribution in the eye tissues. We will consider the **Pennes Bioheat equation** to model the temperature distribution in the eye, coupled with the **radiative transfer equation** (RTE) to model the propagation of light in the eye. For the RTE we will also consider the **fluence equation**, which is derived under the **diffusion approximation**, as well as the **Monte Carlo** approach to simulate the light propagation in the eye.

We will consider a domain Ω representing the human eye, which is composed of 10 subdomains, with boundaries described in Figs. 4 and 5, respectively.

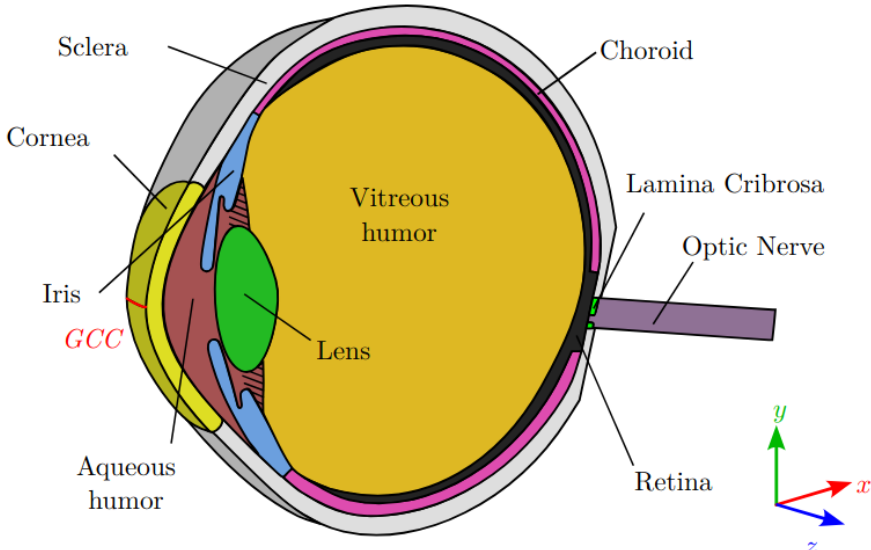


Figure 4: Vertical cut of the geometrical model of the human eye, with the different regions of the eye [SPS24].

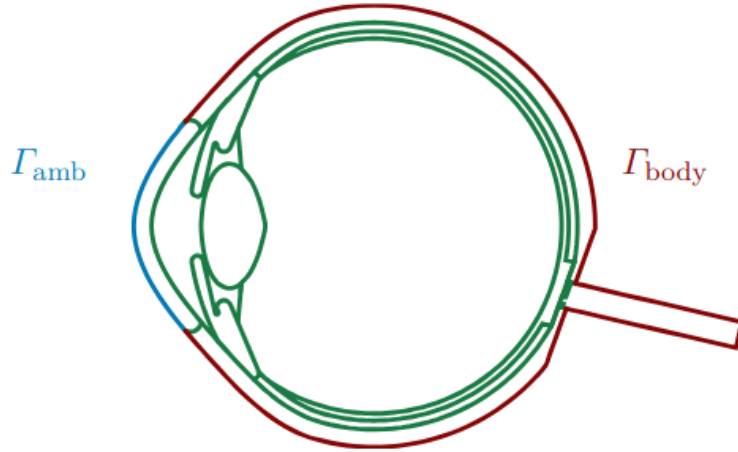


Figure 5: Description of the physical boundaries and interfaces of the domain [SPS24].

3.1 The Pennes Bioheat Equation

The **Pennes bioheat equation** is a mathematical model that describes the heat transfer in biological tissues, taking into account the effects of blood perfusion, metabolic heat generation, and external heat sources. It is given by the following equation:

$$\left\{ \begin{array}{ll} \rho_i C_{p_i} \frac{\partial T_i}{\partial t} - \nabla \cdot (k_i \nabla T_i) = Q_{l,i} + Q_{m,i} + Q_{p,i} & \text{on } \Omega = \bigcup_{i=1}^{10} \Omega_i, \\ -k_i \nabla T_i \cdot n_i = \underbrace{h_{\text{amb}}(T_i - T_{\text{amb}})}_{(i)} + \underbrace{\sigma \varepsilon (T_i^4 - T_{\text{amb}}^4)}_{(ii)} + \underbrace{E}_{(iii)} & \text{on } \Gamma_{\text{amb}}, \\ -k_i \nabla T_i \cdot n_i = h_{\text{bl}}(T_i - T_{\text{bl}}) & \text{on } \Gamma_{\text{body}}, \end{array} \right. \quad (1)$$

where:

- ρ_i is the density of the different materials [kgm^{-3}],
- C_{p_i} is the specific heat capacity of the different materials [$\text{Jkg}^{-1}\text{K}^{-1}$],
- T_i is the temperature of the material [K],
- k_i is the thermal conductivity of the different materials [$\text{Wm}^{-1}\text{K}^{-1}$],
- $Q_{l,i}$ is the laser source term [Wm^{-3}],
- $Q_{m,i}$ is the metabolic heat generation term [Wm^{-3}],
- $Q_{p,i}$ is the perfusion heat generation term [Wm^{-3}],
- h_{amb} is the air-surface heat transfer coefficient [$\text{Wm}^{-2}\text{K}^{-1}$],
- T_{amb} is the ambient temperature [K],

- σ is the Stefan-Boltzmann constant [$\text{Wm}^{-2}\text{K}^{-4}$],
- ε is the emissivity of the surface [dimensionless],
- E is the evaporation rate [Wm^{-2}],
- h_{bl} is the blood-surface heat transfer coefficient [$\text{Wm}^{-2}\text{K}^{-1}$],
- T_{bl} is the blood temperature [K],
- n_i is the normal vector to the surface of the specific material.

The term (i) represents the **convection** heat transfer between the eye surface and the surrounding air, the term (ii) represents the **radiation** heat transfer between the eye surface and the surrounding air, and the term (iii) represents the cooling due to **tears evaporation**.

To ensure we don't have any heat jump at the interfaces between materials, we impose the following **continuity conditions**:

$$\begin{cases} T_i = T_j & \text{on } \Omega_i \cap \Omega_j, \\ k_i \nabla T_i \cdot n_i = -k_j \nabla T_j \cdot n_j & \text{on } \Omega_i \cap \Omega_j. \end{cases} \quad (2)$$

The boundary conditions on Γ_{amb} in (1) represent the heat transfer between the eye surface and the surrounding air. It's **non-linear** and computing intensive, to simplify it, we may consider the approximation proposed in [Sco88b]:

$$\sigma \varepsilon (T^4 - T_{\text{amb}}^4) = (T - T_{\text{amb}}) \underbrace{\sigma \varepsilon (T^2 + T_{\text{amb}}^2)}_{:= h_r}, \quad (3)$$

which allows us to rewrite the boundary condition on Γ_{amb} as:

$$-k \nabla T \cdot n = h_{\text{amb}}(T - T_{\text{amb}}) + h_r(T - T_{\text{amb}}) + E, \quad (4)$$

where h_r is the **radiation heat transfer coefficient** which we will consider as a constant valued at $6 \text{ Wm}^{-2}\text{K}^{-1}$ [SLG06].

If needed, solving the **steady state** of the Pennes equation with $Q_{1,i}$ set to 0 allows us to model the effect of body and environmental interactions on the eye providing an initial condition for the transient simulation.

3.2 The Radiative Transfer Equation (RTE)

The **radiative transfer equation** (RTE) describes the propagation of light in a medium, it is given by:

$$\left(\frac{1}{c} \frac{\partial}{\partial t} + \underbrace{\mathbf{s} \cdot \nabla}_{(i)} + \underbrace{\mu_a(r) + \mu_s(r)}_{(ii)} \right) L(r, s, t) = \underbrace{\mu_s(r) \int_{4\pi} L(r, s', t) \beta(s, s') ds'}_{(iii)} + \underbrace{Q(r, s, t)}_{(iv)}, \quad (5)$$

where:

- $L(r, s, t)$ is the radiance at position r , in direction s , at time t [Wm^{-3}],
- c is the speed of light [ms^{-1}],
- $\mu_a(r)$ is the absorption coefficient at position r [m^{-1}],
- $\mu_s(r)$ is the scattering coefficient at position r [m^{-1}],
- $\beta(s, s')$ is the phase function [dimensionless],
- $Q(r, s, t)$ is the source term [Wm^{-3}].

The **advection** term (i) represent the directional transport of light, the term (ii) represent the **interaction of light** with the medium through **scattering** and **absorption**, the term (iii) represent the **scattering** of light in the medium, and the term (iv) represent and **external source** of light.

The resolution of the RTE is complex and requires accounting for both the directional transport of light and the interaction of light with the medium through processes like scattering, absorption, and emission. The high dimensionality of the problem (involving both spatial coordinates and directional angles) makes solving the full RTE computationally expensive. Approximations are often made, particularly in **scattering-dominated media**.

3.3 The Diffusion Approximation

The **diffusion approximation** of the RTE (also referred to as the *fluence equation*) is derived from the RTE under the diffusion approximation, which is valid when scattering dominates over absorption, *i.e.* when $\mu_a \ll \mu'_s$. In this configuration, multiple scattering events randomize photon directions, and the radiance field becomes nearly isotropic, so light transport can be modeled as a diffusion process rather than directional propagation.

To derive the diffusion approximation, we make two main assumptions:

1. **Nearly isotropic radiance:** After multiple scattering events, the angular distribution of radiance is almost isotropic. This allows us to expand the radiance $L(\mathbf{r}, \mathbf{s}, t)$ in spherical harmonics and retain only the first two terms (P_1 approximation):

$$L(\mathbf{r}, \mathbf{s}, t) \approx \frac{1}{4\pi} \Phi(\mathbf{r}, t) + \frac{3}{4\pi} \mathbf{J}(\mathbf{r}, t) \cdot \mathbf{s},$$

where $\Phi(\mathbf{r}, t) = \int_{4\pi} L d\Omega$ is the fluence rate and $\mathbf{J}(\mathbf{r}, t)$ is the photon current density.

2. **Slowly varying flux:** The fractional change in $\mathbf{J}(\mathbf{r}, t)$ over one transport mean free path is negligible. This allows us to relate the flux directly to the gradient of fluence via Fick's law:

$$\mathbf{J}(\mathbf{r}, t) = -D \nabla \Phi(\mathbf{r}, t), \quad D = \frac{1}{3(\mu_a + \mu'_s)},$$

where D is the diffusion coefficient and $\mu'_s = (1 - g)\mu_s$ is the reduced scattering coefficient.

Substituting Fick's law into the scalar RTE gives the diffusion equation for the fluence:

$$\frac{1}{c} \frac{\partial \Phi(\mathbf{r}, t)}{\partial t} + \mu_a \Phi(\mathbf{r}, t) - \nabla \cdot (D \nabla \Phi(\mathbf{r}, t)) = S(\mathbf{r}, t),$$

where $S(\mathbf{r}, t)$ is an isotropic source term. Notably, only the reduced scattering coefficient μ'_s appears in the diffusion coefficient, meaning that the diffusion behavior is unaffected by changes in the anisotropy g as long as μ'_s remains constant [S R99].

We complete by adding the desired boundary and interface continuity conditions:

$$\left\{ \begin{array}{ll} \frac{1}{c} \frac{\partial \Phi_i}{\partial t} - \nabla \cdot (D_i \nabla \Phi_i) + \mu_a \Phi_i = I_{\text{laser},i} & \text{on } \Omega = \bigcup_{i=1}^{10} \Omega_i, \\ \Phi_i + 2\alpha_i D_i \nabla \Phi_i \cdot n_i = \Phi_{\text{amb}} & \text{on } \Gamma_{\text{amb}}, \\ \Phi_i + 2\alpha_i D_i \nabla \Phi_i \cdot n_i = 0 & \text{on } \partial \Omega_i \setminus \Gamma_{\text{amb}}, \\ \Phi_i = \Phi_j & \text{on } \Omega_i \cap \Omega_j. \end{array} \right. \quad (6)$$

where:

- c is the speed of light [ms^{-1}],
- Φ is the photon fluence rate [Wm^{-2}],
- $D_i = \frac{1}{3(\mu_{a,i} + \mu'_{s,i})}$ is the diffusion coefficient of the different materials [m^2s^{-1}],
- $\mu_{a,i}$ is the absorption coefficient of the different materials [m^{-1}],
- $\mu'_{s,i} = \mu_{s,i}(1 - g)$ is the reduced scattering coefficient of the different materials [m^{-1}],
- g is the anisotropy factor [dimensionless],
- $I_{\text{laser},i}$ is the laser source term [Wm^{-2}],
- Φ_{amb} is the photon fluence rate from ambient light [Wm^{-2}],
- $\alpha_i = \frac{1 + R_i}{1 - R_i}$ is the albedo of the different materials [dimensionless],
- n_i is the normal vector to the surface of the specific material,

- R_i is the coefficient of reflection of the different materials [dimensionless] given by[WT79]:

$$R_i = -1.44n_r^{-2} + 0.7099n_r^{-1} + 0.668 + 0.0636n_r, \quad (7)$$

where n_r denotes the **refraction index** of the surrounding environment.

The Robin boundary conditions on $\partial\Omega_i$ in (6) represents the interaction of light between the two media. The term Φ represent the fluence rate and thus account for the light intensity at the interface, while the term $2\alpha_i D_i \partial_n \Phi$ represents the **diffusion** of light at the interface between the two media. The factor α_i accounts for the reflection of light at the interface which depends on the refraction index n_r of the surrounding environment.

Similarly to the heat equation, to ensure we don't have any fluence jump at the interfaces between materials, we impose the following **continuity conditions**:

$$\Phi_i = \Phi_j \quad \text{on } \Omega_i \cap \Omega_j, \quad (8)$$

at the interface between two adjacent regions Ω_i and Ω_j .

3.4 Pennes and Diffusion Approximation Coupling

We can now use the fluence rate to define the heat generation term Q_1 [Wm^{-3}] in the Pennes equation 1. The heat generation term represents the energy deposited in the tissue by the laser. It is proportional to the absorption coefficient and the photon fluence rate:

$$Q_{\text{laser},i} = \mu_{a,i} \Phi_i.$$

The coupling between the heat and fluence system is then given by:

$$\left\{ \begin{array}{ll} \frac{1}{c} \frac{\partial \Phi_i}{\partial t} - \nabla \cdot (D_i \nabla \Phi_i) + \mu_{a,i} \Phi_i = I_{\text{laser},i} & \text{on } \Omega, \\ \rho_i C_{p,i} \frac{\partial T_i}{\partial t} - \nabla \cdot (k_i \nabla T_i) = Q_{\text{l},i} + Q_{\text{m},i} + Q_{\text{p},i} & \text{on } \Omega, \\ -k_i \nabla T_i \cdot n_i = h_{\text{bl}}(T - T_{\text{bl}}) & \text{on } \Gamma_{\text{body}}, \\ -k_i \nabla T_i \cdot n_i = h_{\text{amb}}(T - T_{\text{amb}}) + h_{\text{r}}(T - T_{\text{amb}}) + E & \text{on } \Gamma_{\text{amb}}, \\ \Phi + 2\alpha_i D_i \nabla \Phi \cdot n_i = \Phi_{\text{amb}} & \text{on } \Gamma_{\text{amb}}, \\ \Phi_i + 2\alpha_i D_i \nabla \Phi_i \cdot n_i = 0 & \text{on } \partial\Omega_i \setminus \Gamma_{\text{amb}}, \\ T_i = T_j & \text{on } \Omega_i \cap \Omega_j, \\ \Phi_i = \Phi_j & \text{on } \Omega_i \cap \Omega_j. \end{array} \right. \quad (9)$$

3.5 Physical Parameters

Physical parameters play a crucial role in determining the behavior of the laser-tissue interaction and the resulting temperature distribution. Values and distributions need to

be researched thoroughly and accurately to ensure precise modeling. Key parameters include the absorption coefficient, scattering coefficient, thermal conductivity, specific heat capacity, and density of the tissue. These parameters influence how the laser energy is absorbed, scattered, and converted into heat within the tissue, ultimately affecting the temperature rise and thermal damage. Table 4 provides a summary of the key physical parameters for modeling laser-tissue interaction, along with baseline values and possible ranges or distributions.

Parameter	Symbol	Units	Baseline Value	Range or Distribution
Absorption Coefficient	μ_a	m^{-1}	50–300	Lognormal or Uniform within range
Reduced Scattering Coefficient	μ'_s	m^{-1}	1000–3000	Uniform or Gaussian (e.g., 1000 ± 300)
Anisotropy Factor	g	—	0.8–0.95	Narrow distribution around mean, e.g., 0.9 ± 0.05
Diffusion Coefficient	$D = \frac{1}{3(\mu_a + \mu'_s)}$	m^2s^{-1}	1×10^{-4}	Derived from μ_a, μ'_s distribution
Photon Fluence Rate	$\Phi(\vec{r}, t)$	Wm^{-2}	Depends on source	Determined by laser power and tissue optics
Laser Source Term	$S(\vec{r}, t)$	Wm^{-3}	Problem-dependent	Based on laser intensity profile
Tissue Density	ρ	kgm^{-3}	1000–1100	Normal distribution (e.g., 1050 ± 50)
Tissue Specific Heat Capacity	c_p	$\text{Jkg}^{-1}\text{K}^{-1}$	3600–4000	Uniform (e.g., 3800 ± 100)
Thermal Conductivity	k	$\text{Wm}^{-1}\text{K}^{-1}$	0.5–0.6	Narrow Gaussian (e.g., 0.55 ± 0.05)
Blood Density	ρ_b	kgm^{-3}	1000–1060	Similar to water (uniform)
Blood Specific Heat Capacity	$c_{p,b}$	$\text{Jkg}^{-1}\text{K}^{-1}$	3600–4000	Similar distribution as tissue c_p
Blood Perfusion Rate	ω_b	s^{-1}	0.001–0.01	Lognormal, depending on vascularization
Arterial Blood Temperature	T_b	K	310 (37°C)	Fixed or normal (310 ± 0.5)
Metabolic Heat Generation	Q_{met}	Wm^{-3}	1000–10,000	Highly variable, lognormal
Laser Heat Generation	$Q_{\text{laser}} = \mu_a \Phi$	Wm^{-3}	Problem-dependent	Derived from μ_a and Φ distributions
Initial Tissue Temperature	$T(\vec{r}, 0)$	K	310	Uniform or normal around baseline
Laser Power	P	W	0.1–10	Determined by laser setup
Beam Waist	w	m	1×10^{-4} – 5×10^{-4}	Determined by laser setup
Laser Focal Point	(m_x, m_y, m_z)	m	Problem-dependent	Determined by laser setup
Refractive Index	n_r	—	1.33–1.42	Uniform or normal distribution

Table 4: Summary of key physical parameters for modeling laser-tissue interaction. Values and distributions are exemplary and should be adjusted based on specific experimental or clinical data.

- Absorption Coefficient (μ_a)
 - Depends on laser wavelength and tissue type.
 - Given in Table 5 for various ocular tissues at 577 nm.
- Reduced Scattering Coefficient (μ'_s) [WV10]
 - Accounts for the scattering events that effectively change the direction of photon propagation.
 - Ocular tissues exhibit μ'_s values ranging from 1000 to 3000 m^{-1} , depending on the type of tissue and wavelength.
 - For ocular fluid, the reduced scattering coefficient is typically low and can be approximated by the reduced scattering coefficient of water which is negligible.
- Anisotropy Factor (g) [WV10]
 - Indicates the average cosine of the scattering angle; values close to 1 imply forward-directed scattering.
 - For ocular tissues, g typically ranges from 0.8 to 0.95.
- Diffusion Coefficient (D):

- Describes the rate at which light diffuses through tissue.
- Derived from $D = \frac{1}{3(\mu_a + \mu'_s)}$.
- Refractive Index (n_r):
 - Determines the speed of light in the medium.
 - Given in Table 6 for various ocular tissues at 577 nm.
- The other parameters are discussed in [Sai24] and [Zan+25].

Note that we chose to use the absorption coefficient and refractive index for a 577 nm wavelength since it's considered the best for diabetic retinopathy treatment [Afl+20b].

Table 5: Values of absorption coefficient at 577 nm.

Tissue	Absorption coefficient (cm^{-1})	Extinction coefficient κ (-)	Sample type	Reference
Cornea	0.23	1.045	animal	Regal <i>et al</i> [Reg+19]
Aqueous Humour	0.47	2.144	animal	Regal <i>et al</i> [Reg+19]
Iris	28.02	1.287	animal	Regal <i>et al</i> [Reg+19]
Ciliary Body	0.08	3.747	human	Cvetković <i>et al</i> [CPP08]
Lens—Anterior Part	0.05	2.186	animal	Regal <i>et al</i> [Reg+19]
Lens—Posterior Part	0.05	2.186	animal	Regal <i>et al</i> [Reg+19]
Vitreous Humour	0.47	2.144	animal	Regal <i>et al</i> [Reg+19]
Retina	5.94	2.728	human	Cvetković <i>et al</i> [CPP08]
RPE	1000.0	4.592	animal	Aflalo <i>et al</i> [Afl+20a]
Choroid	35.59	1.634	animal	Regal <i>et al</i> [Reg+19]
Sclera	3.55	1.630	animal	Regal <i>et al</i> [Reg+19]

Table 6: Refractive index of eye tissues at 577 nm.

Tissue	Refractive index (n)	Sample type	Reference
Cornea	1.375	human	Liou and Brennan [LB97]
Aqueous Humour	1.335	human	Liou and Brennan [LB97]
Iris	1.385	animal	Regal et al. [Reg+19]
Ciliary Body	1.380	—	Nemati [NRW96]
Lens—Anterior Part ^a	Grad A	human	Liou and Brennan [LB97]
Lens—Posterior Part ^b	Grad P	human	Liou and Brennan [LB97]
Vitreous Humour	1.335	human	Liou and Brennan [LB97]
Retina	1.377	animal	Enping [Enp93]
RPE	1.377	animal	Enping [Enp93]
Choroid	1.356	animal	Regal et al. [Reg+19]
Sclera	1.366	animal	Regal et al. [Reg+19]

$$^a \text{Grad A} = 1.367 + 0.049057z - 0.015427z^2 - 0.001978w^2$$

$$^b \text{Grad P} = 1.406 - 0.006605z^2 - 0.001978w^2$$

Additionally, laser settings such as the **power**, **wavelength** and **duration** can greatly vary depending on the type of eye disease being treated, in the Table 7 we present some common laser treatment methods used for eye diseases.

Table 7: Common laser treatment methods used for eye diseases [Nar17].

Treatment	Disease	Target	Laser	Interaction
LASIK	Vision correction	Cornea	Excimer (0.1 MW, 1 mJ, 10–20 ns)	Vaporization, shaping
Capsulotomy	Cataract	Lens	Nd:YAG	Ablation
Vitreolysis	Vitreous hemorrhage	Vitreous humor	Nd:YAG	Vaporization
Retinal surgery	Retinal diseases	Retina, sclera	Nd:YAG (0.2–0.5 W, 100–200 ms)	Photocoagulation (60°C)
TTT	Tumors (melanoma)	Posterior eye	IR diode	Thermal effect

4 Mathematical and Computational Framework

In this chapter we presents the mathematical and computational tools used to model light propagation and heat transfer in biological tissues. The first part introduces the Monte Carlo method for solving the Radiative Transfer Equation (RTE-MC), describing the main mechanisms of photon propagation, scattering, absorption, and interface interactions, as well as techniques such as Russian Roulette to efficiently manage photon weights.

Next, we discuss the coupling of the RTE-MC solution with the Pennes bioheat equation, which allows the evaluation of temperature distributions induced by laser irradiation. The chapter then develops the variational formulations of both the heat equation and the diffusion approximation, providing a foundation for numerical discretization.

Finally, the chapter details the finite element discretization of the governing equations and the temporal schemes employed for time-dependent simulations.

4.1 The Monte Carlo Method (RTE-MC)

As we saw the RTE is complex and requires accounting for both the directional transport of light and the interaction of light with the medium through processes like scattering, absorption, and emission. The high dimensionality of the problem (involving both spatial coordinates and directional angles) makes solving the full RTE computationally expensive. Approximations are often made, particularly in **scattering-dominated media** like we did with the **diffusion approximation**, the downside of this approximation is that it is not valid in all cases, especially when the absorption coefficient is high like in the retina. Indeed, the retinal pigmented epithelium (RPE) is known to have a very high absorption coefficient, making the diffusion approximation less accurate. Another approach to solve the RTE is to use a **Monte Carlo based method** which is a statistical method that simulates the propagation of photons through a medium by tracking the paths of packet of photons. This method is particularly useful for simulating light propagation in complex geometries and heterogeneous media, such as biological tissues. The Monte Carlo method is based on the principle of **random sampling** and uses a large number (millions) of simulated photons to estimate the light distribution in the medium.

4.1.1 Photon Propagation

We start by defining the attenuated energy E_{att} as the sum of the absorbed energy E_{absorb} and the scattered energy E_{scatt} :

$$E_{\text{att}} = E_{\text{absorb}} + E_{\text{scatt}}. \quad (10)$$

We then use the **Beer-Lambert law** to describe the attenuated energy, for a uniform medium of length x under the influence of a monochromatic light source of N_0 photons, the number of transmitted photons N_x is given by:

$$N_x = N_0 e^{-\mu_a x} e^{-\mu_s x}, \quad (11)$$

where μ_a is the **absorption coefficient** and μ_s is the **scattering coefficient**. Posing the coefficient of attenuation as $\mu_t = \mu_a + \mu_s$, we can rewrite the equation as:

$$N_x = N_0 e^{-\mu_t x}. \quad (12)$$

We then compute the distance x the photon travels before being absorbed or scattered using the **exponential distribution**, we start by showing that the **cumulative distri-**

bution function (**CDF**) of the exponential distribution is invertible:

$$\begin{aligned}
f_x(x) &= \mu_t e^{-\mu_t x} \mathbb{1}_{\{x \geq 0\}} \\
F_x(x) &= \int_{-\infty}^x f_x(t) dt = \int_0^x \mu_t e^{-\mu_t t} dt \\
&= \mu_t \left[-\frac{1}{\mu_t} e^{-\mu_t t} \right]_0^x \\
&= 1 - e^{-\mu_t x} \mathbb{1}_{\{x \geq 0\}}
\end{aligned} \tag{13}$$

which strictly decrease in \mathbb{R}^+ and thus is indeed invertible. This inverse is given by:

$$\begin{aligned}
y &= 1 - e^{-\mu_t x} \quad y \in (0, 1) \\
e^{-\mu_t x} &= 1 - y \\
-\mu_t x &= \ln(1 - y)
\end{aligned} \tag{14}$$

Since $y \in (0, 1)$, we have $\xi = 1 - y \in (0, 1)$ and thus:

$$s := x = -\frac{\ln(\xi)}{\mu_t} \tag{15}$$

Where ξ is a random number uniformly distributed in $(0, 1)$ and s is the distance traveled by the photon in the medium.

Explanation: This *inverse transform sampling* allows us to generate random photon path lengths that follow the correct exponential distribution. By drawing a uniform random number ξ and applying the inverse CDF, each photon is assigned a physically consistent free path.

4.1.2 Photon Scattering

For the scattering process, we use a **phase function** $p(\theta)$ which describes the angular distribution of light scattering. It represents the probability that a photon, upon interacting with a medium, is scattered into a direction defined by the angle θ (and ϕ if considering the full 3D case). This function is normalized such that

$$\int_{\Omega} p(\theta, \phi) d\Omega = 1,$$

where the integration is over the entire solid angle.

A commonly used phase function in Monte Carlo photon transport is the **Henyey-Greenstein (HG) phase function** [HG41; SB03]:

$$p(\cos \theta) = \frac{1 - g^2}{(1 + g^2 - 2g \cos \theta)^{3/2}},$$

where $g = \langle \cos \theta \rangle \in [-1, 1]$ is the **anisotropy** factor representing the degree of forward scattering. This function effectively captures the anisotropic scattering empirically observed in many biological tissues. This function is also a density of probability, indeed,

if $u := \cos \theta$, we have $\forall u \in (-1, 1), p(u) > 0$ and,

$$\int_{\mathbb{R}} p(u) du = \frac{1-g^2}{2} \int_{-1}^1 \frac{1-g^2}{(1+g^2-2gu)^{3/2}} du \quad (16)$$

$$= \frac{1-g^2}{2} \left[\frac{1}{g\sqrt{1+g^2-2gu}} \right]_{-1}^1 \quad (17)$$

$$= \frac{1-g^2}{2} \left[\frac{1}{\sqrt{1+g^2-2g}} - \frac{1}{\sqrt{1+g^2+2g}} \right] \quad (18)$$

$$= \frac{1-g^2}{2} \left[\frac{1}{\sqrt{(1-g)^2}} - \frac{1}{\sqrt{(1+g)^2}} \right] \quad (19)$$

$$= \frac{2g(1-g^2)}{2g(1-g(1+g))} \quad (20)$$

$$= 1. \quad (21)$$

Its cumulative distribution function (CDF) is given by:

$$F(u) = \int_{-\infty}^t p(u) du \quad (22)$$

$$= \frac{1-g^2}{2} \int_{-1}^t \frac{1}{\sqrt{1+g^2-2gu}} du \quad (23)$$

$$= \frac{1-g^2}{2} \left[\frac{1}{g\sqrt{1+g^2-2gu}} \right]_{-1}^t \quad (24)$$

$$= \frac{1-g^2}{2} \left[\frac{1}{\sqrt{(1+g^2-2gu)}} - \frac{1}{\sqrt{(1+g^2+2g)}} \right] \quad (25)$$

We have that $F(u)$ is strictly increasing in $(-1, 1)$ and thus is invertible. The inverse is given by:

$$y = \frac{1-g^2}{2} \left[\frac{1}{\sqrt{1+g^2-2gu}} - \frac{1}{\sqrt{1+g^2+2g}} \right] \quad (26)$$

$$\Leftrightarrow \frac{2yg}{1-g^2} = \frac{1}{\sqrt{1+g^2-2gu}} - \frac{1}{1+g} \quad (27)$$

$$\Leftrightarrow \frac{2yg}{1-g^2} + \frac{1}{1+g} = \frac{1}{\sqrt{1+g^2-2gu}} \quad (28)$$

$$\Leftrightarrow \left(\frac{2yg(1+g) + (1-g^2)}{(1-g^2)(1+g)} \right)^2 = \frac{1}{1+g^2-2gu} \quad (29)$$

$$\Leftrightarrow \left(\frac{(1+g)(1-g^2)}{2yg(1+g) + (1-g^2)} \right)^2 = 1+g^2-2gu \quad (30)$$

$$\Leftrightarrow u = \frac{1}{2g} \left(1+g^2 - \left(\frac{1-g^2}{2yg+1-g} \right)^2 \right) \quad (31)$$

Let X be a random variable uniformly distributed in $(0, 1)$, we can sample the angle θ using the inverse of the CDF:

$$\cos \theta = \begin{cases} 2X - 1, & \text{if } g \approx 0, \\ \frac{1 + g^2 - \left(\frac{1-g^2}{1-g+2gX}\right)^2}{2g}, & \text{otherwise,} \end{cases} \quad (32)$$

and thus:

$$\theta = \arccos \left(\frac{1}{2g} \left(1 + g^2 - \left(\frac{1-g^2}{2gX+1-g} \right)^2 \right) \right). \quad (33)$$

The scattering angle θ is then used to update the direction of the photon after scattering:

$$\text{photon direction}(x, y, z) = \begin{cases} \sin(\theta) \sin(\phi) \\ \sin(\theta) \cos(\phi) \\ \cos(\theta) \end{cases} \quad (34)$$

where ϕ is the **azimuthal angle**, which can be sampled uniformly in $[0, 2\pi]$. The new position is then given by:

$$\begin{aligned} x' &= x + s \sin(\theta) \cos(\phi) \\ y' &= y + s \sin(\theta) \sin(\phi) \\ z' &= z + s \cos(\theta) \end{aligned} \quad (35)$$

4.1.3 Photon Absorption

When space is discretized into a mesh, the photon will travel through the mesh and deposit energy in the elements it traverses before eventually reaching an interface or exiting the medium. The intersection between the photon path and the mesh elements are located using a **Bounding Volume Hierarchy** (BVH) data structure, which allows us to efficiently find the next intersection point with the mesh elements. The energy deposited in each element is given by:

$$A_i = w \cdot \frac{\mu_a}{\mu_t} \cdot (1 - e^{-\mu_t \cdot \Delta s_i})$$

where:

- A_i : is the **energy deposited in element i**
- w : is the **weight (i.e. the energy) of the photon** (initialized at 1),
- $\mu_t = \mu_a + \mu_s$: is the **total attenuation**,
- Δs_i : is the **path length in element i** .

The remaining weight of the photon after absorption is updated as:

$$w \leftarrow w \cdot e^{-\mu_t \cdot \Delta s_i}$$

This loop runs until the photon reaches an interface or exhausts its path. If the ray continues beyond the last known intersection we consider the **tail segment** of the step, which is the remaining distance to the last intersection point:

$$A_{\text{tail}} = w \cdot \frac{\mu_a}{\mu_t} \cdot (1 - e^{-\mu_t \cdot s_{\text{tail}}})$$

where:

- $s_{\text{tail}} = s - t_{\text{last}}$: is the **remaining distance**,
- A_{tail} : is the **energy deposited in tail element**,
- $w \leftarrow w \cdot e^{-\mu_t \cdot s_{\text{tail}}}$: is the **update weight**.

If the tail lies in a valid mesh element, the energy is deposited and the photon advances. This ensures all traversed regions contribute to absorption, including the “tail” of the step.

4.1.4 Interface Handling

When a photon reaches an interface, we need to determine whether it is transmitted or reflected as shown in Figure 6.

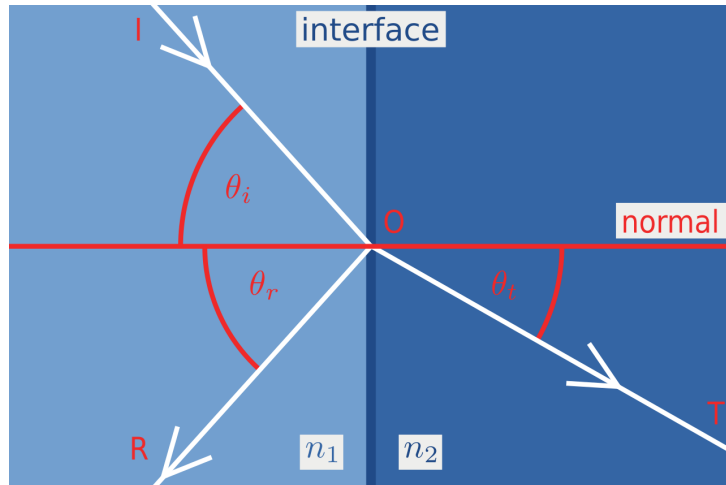


Figure 6: Fresnel equations illustrated ($\theta_i = \theta_r$) (Wikipedia)

where,

- θ_i is the angle of incidence,
- θ_r is the angle of reflection,
- θ_t is the angle of transmission.

This decision is made using the **Fresnel equations** which describe the reflection and transmission of light at an interface between two media with different refractive indices. The Fresnel equations give the reflection and transmission coefficients for both perpendicular and parallel polarizations of light. The coefficients are given by:

$$R_{\perp} = \left| \frac{n_1 \cos(\theta_i) - n_2 \cos(\theta_r)}{n_1 \cos(\theta_i) + n_2 \cos(\theta_r)} \right|^2, \quad (36)$$

$$R_{\parallel} = \left| \frac{n_1 \cos(\theta_i) - n_2 \cos(\theta_r)}{n_1 \cos(\theta_i) + n_2 \cos(\theta_r)} \right|^2, \quad (37)$$

where:

- n_1 and n_2 are the refractive indices of the two media,
- θ_i is the angle of incidence in the first medium,
- θ_r is the angle of refraction in the second medium, which can be computed using Snell's law:

$$n_1 \sin(\theta_i) = n_2 \sin(\theta_r). \quad (38)$$

We neglect the polarization of the light and consider the average of the two coefficients, the probabilities of reflection and transmission are then given by:

$$P_{\text{reflect}} = \frac{R_{\perp} + R_{\parallel}}{2}. \quad (39)$$

$$P_{\text{transmit}} = 1 - P_{\text{reflect}}. \quad (40)$$

To improve computation speed while keeping accuracy, we will use the **Schlick approximation**[21] instead of the Fresnel equations to compute the reflection coefficient:

$$R = R_0 + (1 - R_0)(1 - \cos(\theta))^5, \quad (41)$$

where R_0 is the reflectance at normal incidence, given by:

$$R_0 = \left(\frac{n_1 - n_2}{n_1 + n_2} \right)^2. \quad (42)$$

Using the Schlick approximation allows us to compute the reflection coefficient more efficiently which can be crucial for real-time applications, our average absolute mean error of the Schlick approximation compared to the Fresnel equations is around 0.044269 (*cf.* Appendix 9).

If the photon is reflected, we update its direction using the reflection law:

$$\text{photon direction}(x, y, z) = \begin{cases} \sin(\theta) \sin(\phi) \\ \sin(\theta) \sin(\phi) \\ -\cos(\theta) \end{cases} \quad (43)$$

If the photon is transmitted, we update its direction using Snell's law:

$$\text{photon direction}(x, y, z) = \begin{cases} \sin(\theta_r) \sin(\phi) \\ \sin(\theta_r) \sin(\phi) \\ \cos(\theta_r) \end{cases} \quad (44)$$

The new position is then given by:

$$\begin{aligned}x' &= x + s \sin(\theta) \cos(\phi) \\y' &= y + s \sin(\theta) \sin(\phi) \\z' &= z + s \cos(\theta)\end{aligned}\tag{45}$$

4.1.5 Russian Roulette

As the photon propagates and undergoes multiple interactions, its weight w (representing its energy) typically decreases rapidly due to absorption and scattering events. Tracking all low-weight photons is computationally inefficient and often contributes negligibly to the overall solution.

To mitigate this while preserving statistical correctness, we employ the **Russian Roulette** technique. When the photon's weight falls below a predefined threshold w_{\min} , we stochastically decide whether to terminate the photon or allow it to continue with a renormalized weight.

Let $p \in (0, 1)$ be the survival probability. The algorithm proceeds as follows:

Algorithm 1 Russian Roulette

Require: Photon weight w , minimum weight threshold w_{\min} , survival probability p

```

1: if  $w < w_{\min}$  then
2:   Sample a realization  $\xi \sim \mathcal{U}(0, 1)$ 
3:   if  $\xi < p$  then
4:     Photon survives:  $w \leftarrow \frac{w}{p}$ 
5:   else
6:     Photon is terminated
7:   end if
8: else
9:   Photon continues with weight  $w$ 
10: end if

```

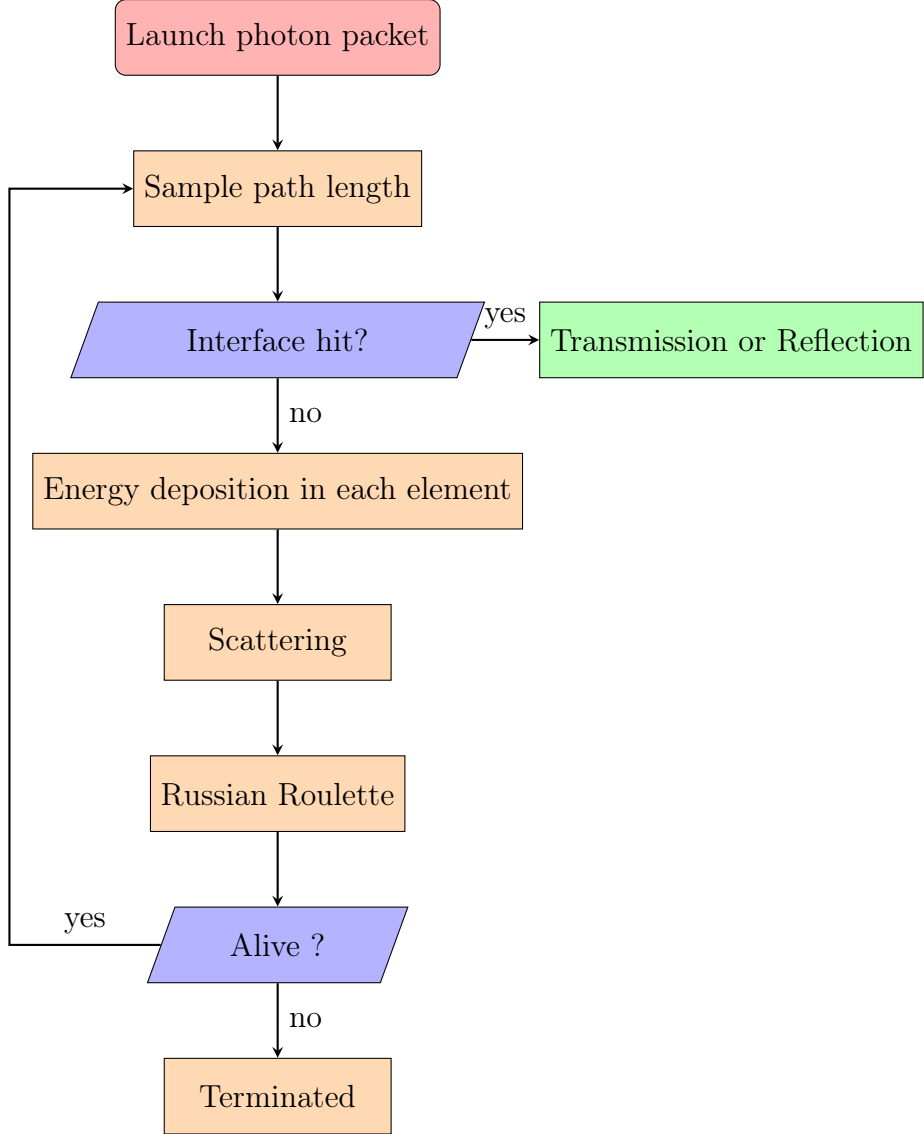
This method ensures energy conservation in expectation:

$$\mathbb{E}[w_{\text{after}}] = p \cdot \frac{w}{p} + (1 - p) \cdot 0 = w,$$

which maintains the unbiased nature of the Monte Carlo simulation.

4.1.6 RTE-MC Summary

The process of the Monte Carlo method for solving the RTE can be summarized in the following flowchart:



4.2 Pennes Bioheat and RTE-MC Coupling

We can now couple the RTE-MC with the Pennes bioheat equation to model the interaction of laser light with biological tissues on the domain $\Omega = \bigcup_{i=1}^{10} \Omega_i$:

$$\begin{cases} \rho C_{p,i} \frac{\partial T_i}{\partial t} - \nabla \cdot (k_i \nabla T_i) = S + Q_{m,i} + Q_{p,i} & \text{on } \Omega, \\ S = PA \end{cases} \quad (46)$$

where P is the power of the laser [W] and A is the **normalized absorption map** obtained by solving the RTE-MC.

4.3 The Variational Formulation

In this section, we derive the variational formulation of the heat and fluence equations. This approach is obtained by multiplying the PDEs by test functions and integrating

over the domain, ensuring the equations are satisfied in a weak sense. Integration by parts (divergence theorem) reduces the order of derivatives, and boundary conditions are naturally incorporated. This formulation is fundamental for numerical methods like FEM and provides a framework for proving solution properties such as existence and stability. Since Φ and T both require finite energy and well-defined gradients, we will consider them in the following functional spaces:

$$H^1(\Omega) = \{v \in L^2(\Omega) \mid \nabla v \in L^2(\Omega)\},$$

known as the **H^1 Sobolev space**.

4.3.1 The Variational Formulation of the Heat Equation

Let $v \in H^1(\Omega)$ be a test function, we have:

$$\sum_i \left[\int_{\Omega_i} \rho_i C_{p_i} \frac{\partial T_i}{\partial t} v \, dx - \int_{\Omega_i} k_i \nabla T_i \cdot \nabla v \, dx \right] = \sum_i \int_{\Omega_i} \mu_{a_i} \Phi_i v \, dx,$$

applying Green's theorem (divergence theorem) yields:

$$\sum_i \left[\int_{\Omega_i} \rho_i C_{p_i} \frac{\partial T_i}{\partial t} v \, dx - \int_{\partial \Omega_i} k_i v \nabla T_i \cdot n_i \, ds + \int_{\Omega_i} k_i \nabla v \cdot \nabla T_i \, dx \right] = \sum_i \int_{\Omega_i} v \mu_{a_i} \Phi_i \, dx.$$

applying the boundary and interface conditions from (1) and (2), yields:

$$\begin{aligned} & \sum_i \int_{\Omega_i} \rho_i C_{p_i} \frac{\partial T_i}{\partial t} v \, dx + \int_{\Gamma_{\text{body}}} v \underbrace{h_{\text{bl}}(T_i - T_{\text{bl}})}_{=h_{\text{bl}}T_i - h_{\text{bl}}T_{\text{bl}}} \, ds + \int_{\Gamma_{\text{amb}}} v \underbrace{h_{\text{amb}}(T_i - T_{\text{amb}})}_{=h_{\text{amb}}T_i - h_{\text{amb}}T_{\text{amb}}} \, ds \\ & + \int_{\Gamma_{\text{amb}}} v \underbrace{h_{\text{r}}(T_i - T_{\text{amb}})}_{=h_{\text{r}}T_i - h_{\text{r}}T_{\text{amb}}} + E \, ds - \sum_i \int_{\partial \Omega_i \setminus \{\Gamma_{\text{amb}} \cup \Gamma_{\text{body}}\}} v k_i \nabla T_i \cdot n_i \, ds \\ & + \sum_i \int_{\Omega_i} k_i \nabla v \cdot \nabla T_i \, dx = \sum_i \int_{\Omega_i} v \mu_{a_i} \Phi_i \, dx. \end{aligned}$$

which we can rewrite as:

$$\begin{aligned} & \sum_i \int_{\Omega_i} \rho_i C_{p_i} \frac{\partial T_i}{\partial t} v \, dx + \int_{\Gamma_{\text{body}}} v h_{\text{bl}} T_i \, ds + \int_{\Gamma_{\text{amb}}} v [h_{\text{amb}} T_i + h_{\text{r}} T_i] \, ds \\ & - \sum_i \int_{\partial \Omega_i \setminus \{\Gamma_{\text{amb}} \cup \Gamma_{\text{body}}\}} k_i \nabla T_i \cdot n_i \, ds + \sum_i \int_{\Omega_i} k_i \nabla v \cdot \nabla T_i \, dx = \int_{\Gamma_{\text{body}}} v h_{\text{bl}} T_{\text{bl}} \, ds \\ & + \int_{\Gamma_{\text{amb}}} v [h_{\text{amb}} T_{\text{amb}} + h_{\text{r}} T_{\text{amb}} - E] \, ds + \sum_i \int_{\Omega_i} v \mu_{a_i} \Phi_i \, dx. \end{aligned}$$

We pose:

$$\begin{aligned} a_T(T, v) &= \sum_i \int_{\Omega_i} \rho_i C_{p_i} \frac{\partial T_i}{\partial t} v \, dx + \int_{\Gamma_{\text{body}}} v h_{\text{bl}} T_i \, ds + \int_{\Gamma_{\text{amb}}} v [h_{\text{amb}} T_i + h_{\text{r}} T_i] \, ds \\ & - \sum_i \int_{\partial \Omega_i \setminus \{\Gamma_{\text{amb}} \cup \Gamma_{\text{body}}\}} k_i \nabla T_i \cdot n_i \, ds + \sum_i \int_{\Omega_i} k_i \nabla v \cdot \nabla T_i \, dx, \\ l_T(v) &= \int_{\Gamma_{\text{body}}} v h_{\text{bl}} T_{\text{bl}} \, ds + \int_{\Gamma_{\text{amb}}} v [h_{\text{amb}} T_{\text{amb}} + h_{\text{r}} T_{\text{amb}} - E] \, ds + \sum_i \int_{\Omega_i} v \mu_{a_i} \Phi_i \, dx. \end{aligned}$$

4.3.2 The Variational Formulation of the DA

Let $v \in H^1(\Omega)$ be a test function, we have:

$$\sum_i \left[\int_{\Omega_i} \frac{1}{c} \frac{\partial \Phi_i}{\partial t} v \, dx - \int_{\Omega_i} \nabla \cdot (D_i \nabla \Phi_i) v \, dx + \int_{\Omega_i} \mu_{a_i} \Phi_i v \, dx \right] = \sum_i \int_{\Omega_i} I_{\text{laser},i} v \, dx,$$

applying Green's theorem (divergence theorem) yields:

$$\sum_i \left[\int_{\Omega_i} \frac{1}{c} \frac{\partial \Phi_i}{\partial t} v \, dx - \int_{\partial \Omega_i} v D_i \nabla \Phi_i \cdot n_i \, ds + \int_{\Omega_i} D_i \nabla v \cdot \nabla \Phi_i \, dx + \int_{\Omega_i} \mu_{a_i} \Phi_i v \, dx \right] = \sum_i \int_{\Omega_i} I_{\text{laser},i} v \, dx,$$

applying the boundary and interface conditions from (6) yields:

$$\begin{aligned} & \sum_i \int_{\Omega_i} \frac{1}{c} \frac{\partial \Phi_i}{\partial t} v \, dx + \int_{\Gamma_{\text{amb}}} v \frac{\Phi_{\text{amb}} - \Phi_i}{2\alpha_i} \, ds + \sum_i \int_{\partial \Omega_i \setminus \Gamma_{\text{amb}}} v \frac{\Phi_i}{2\alpha_i} \, ds \\ & + \sum_i \int_{\Omega_i} D_i \nabla v \cdot \nabla \Phi_i \, dx + \sum_i \int_{\Omega_i} \mu_{a_i} \Phi_i v \, dx = \sum_i \int_{\Omega_i} I_{\text{laser},i} v \, dx. \end{aligned}$$

which we can rewrite as:

$$\begin{aligned} & \sum_i \int_{\Omega_i} \frac{1}{c} \frac{\partial \Phi_i}{\partial t} v \, dx - \int_{\Gamma_{\text{amb}}} v \frac{\Phi_i}{2\alpha_i} \, ds + \sum_i \int_{\partial \Omega_i \setminus \Gamma_{\text{amb}}} v \frac{\Phi_i}{2\alpha_i} \, ds \\ & + \sum_i \int_{\Omega_i} D_i \nabla v \cdot \nabla \Phi_i \, dx + \sum_i \int_{\Omega_i} \mu_{a_i} \Phi_i v \, dx = \sum_i \int_{\Omega_i} I_{\text{laser},i} v \, dx - \int_{\Gamma_{\text{amb}}} v \frac{\Phi_{\text{amb}}}{2\alpha_i} \, ds. \end{aligned}$$

We pose:

$$\begin{aligned} a_{\Phi}(\Phi, v) &= \sum_i \int_{\Omega_i} \frac{1}{c} \frac{\partial \Phi_i}{\partial t} v \, dx - \int_{\Gamma_{\text{amb}}} v \frac{\Phi_i}{2\alpha_i} \, ds + \sum_i \int_{\partial \Omega_i \setminus \Gamma_{\text{amb}}} v \frac{\Phi_i}{2\alpha_i} \, ds \\ & + \sum_i \int_{\Omega_i} D_i \nabla v \cdot \nabla \Phi_i \, dx + \sum_i \int_{\Omega_i} \mu_{a_i} \Phi_i v \, dx, \\ l_{\Phi}(v) &= \sum_i \int_{\Omega_i} I_{\text{laser},i} v \, dx - \int_{\Gamma_{\text{amb}}} v \frac{\Phi_{\text{amb}}}{2\alpha_i} \, ds. \end{aligned}$$

The variational formulation of the problem is then: Find $T \in H^1(\Omega)$ and $\Phi \in H^1(\Omega)$ such that for all test functions $v \in H^1(\Omega)$:

$$a_T(T, v) = l_T(v; \Phi), \quad a_{\Phi}(\Phi, v) = l_{\Phi}(v). \quad (47)$$

Theorem 1. (*Existence and Uniqueness*). *The variational formulation (47) has a unique solution $(T, \Phi) \in H^1(\Omega) \times H^1(\Omega)$.*

Proof. To show :

- $a_T(T, v)$ is bilinear, continuous and coercive,

- $l_T(v; \Phi)$ is linear and continuous,
- $a_\Phi(\Phi, v)$ is bilinear, continuous and coercive,
- $l_\Phi(v)$ is linear and continuous.

Apply the Lax-Milgram theorem to conclude. \square

4.4 Finite Element Discretization

The idea of the Finite Element Method (FEM) is to approximate continuous solutions Φ and T on a finite dimensional space $V_h \in H_\Omega^1$ spanned by a set of basis functions $\{\psi_j\}, j = 1, \dots, \mathcal{N}$.

Since T and Φ belong to the same functional space $H^1(\Omega)$ their FEM approximation are given by decomposing them as a linear combination of same the basis functions:

$$T_h = \sum_{j=1}^{\mathcal{N}} T_j^{\text{fem}} \psi_j, \quad \Phi_h = \sum_{j=1}^{\mathcal{N}} \Phi_j^{\text{fem}} \psi_j.$$

The results of the Galerkin approximation is a finite-dimensional equivalent of the variational formulation. The goal is to find $T_h \in V_h$ and $\Phi_h \in V_h$ such that:

$$\begin{aligned} a_T(T_h, v_h) &= l_T(v_h) \quad \forall v_h \in V_h, \\ a_\Phi(\Phi_h, v_h) &= l_\Phi(v_h) \quad \forall v_h \in V_h. \end{aligned}$$

Which leads to:

$$\begin{aligned} a_T(T_h, \psi_j) &= l_T(\psi_j) \quad \forall j = 1, \dots, \mathcal{N}, \\ a_\Phi(\Phi_h, \psi_j) &= l_\Phi(\psi_j) \quad \forall j = 1, \dots, \mathcal{N}. \end{aligned}$$

We define the mass matrix \mathbf{M} , the stiffness matrices \mathbf{A}_T and \mathbf{A}_Φ , the right-hand side vectors \mathbf{L}_T and \mathbf{L}_Φ :

$$\begin{aligned} \mathbf{M} &= \left[\int_{\Omega_i} \psi_i \psi_j \, dx \right]_{i,j} \in \mathbb{R}^{\mathcal{N} \times \mathcal{N}}, \\ \mathbf{A}_T &= \left[\int_{\Omega_i} k_i \nabla \psi_i \cdot \nabla \psi_j \, dx + \int_{\Gamma_{\text{body}}} h_{\text{bl}} \psi_i \psi_j \, ds + \int_{\Gamma_{\text{amb}}} (h_{\text{amb}} + h_r) \psi_i \psi_j \, ds \right]_{i,j} \in \mathbb{R}^{\mathcal{N} \times \mathcal{N}}, \\ \mathbf{A}_\Phi &= \left[\int_{\Omega_i} D_i \nabla \psi_i \cdot \nabla \psi_j \, dx + \int_{\Gamma_{\text{amb}}} \frac{\psi_i \psi_j}{2\alpha_i} \, ds \right]_{i,j} \in \mathbb{R}^{\mathcal{N} \times \mathcal{N}}, \\ \mathbf{L}_T &= \left[\int_{\Omega_i} \mu_{a_i} \Phi_i \psi_j \, dx + \int_{\Gamma_{\text{body}}} h_{\text{bl}} T_{\text{bl}} \psi_j \, ds + \int_{\Gamma_{\text{amb}}} (h_{\text{amb}} T_{\text{amb}} + h_r T_{\text{amb}} - E) \psi_j \, ds \right]_j \in \mathbb{R}^{\mathcal{N}}, \\ \mathbf{L}_\Phi &= \left[\int_{\Omega_i} S \psi_j \, dx - \int_{\Gamma_{\text{amb}}} \frac{\Phi_{\text{amb}} \psi_j}{2\alpha_i} \, ds \right]_j \in \mathbb{R}^{\mathcal{N}}. \end{aligned}$$

We can write then the system of equations in the **algebraic form**:

For the fluence:

$$\mathbf{M} \frac{\partial \Phi^{\text{fem}}}{c \partial t} + \mathbf{A}_\Phi \Phi^{\text{fem}} = \mathbf{L}_\Phi.$$

And for the heat:

$$\rho C_p \mathbf{M} \frac{\partial \mathbf{T}^{\text{fem}}}{\partial t} + \mu_a \mathbf{M} \Phi^{\text{fem}} = \mathbf{L}_T.$$

Feel++ [Pru+24] solve these systems in a monolithic block of the form:

$$\begin{bmatrix} \mathbf{M} & 0 \\ 0 & \rho C_p \mathbf{M} \end{bmatrix} \begin{bmatrix} \frac{\partial \Phi^{\text{fem}}}{c \partial t} \\ \frac{\partial \mathbf{T}^{\text{fem}}}{\partial t} \end{bmatrix} + \begin{bmatrix} \mathbf{A}_\Phi & 0 \\ 0 & \mu_a \mathbf{M} \end{bmatrix} \begin{bmatrix} \Phi^{\text{fem}} \\ \mathbf{T}^{\text{fem}} \end{bmatrix} = \begin{bmatrix} \mathbf{L}_\Phi \\ \mathbf{L}_T \end{bmatrix}.$$

4.5 Time Scheme

To solve the time-dependent model using the Finite Element Method (FEM), we discretize both the time and spatial domains. Let Δt represent the time step size, and define $t^n = n\Delta t$ for $n = 0, 1, 2, \dots, N$, where N is the total number of time steps. The PDEs are solved iteratively for each time step.

4.6 Heat Equation Discretization

The time-dependent heat equation is:

$$\rho C_p \mathbf{M} \frac{\partial \mathbf{T}^{\text{fem}}}{\partial t} + \mu_a \mathbf{M} \Phi^{\text{fem}} = \mathbf{L}_T.$$

Using the finite difference scheme for the time derivative:

$$\frac{\partial \mathbf{T}^{\text{fem}}}{\partial t} \approx \frac{\mathbf{T}^{n+1} - \mathbf{T}^n}{\Delta t},$$

We then substitute this approximation into the heat equation to get:

$$\rho C_p \mathbf{M} \frac{\mathbf{T}^{n+1} - \mathbf{T}^n}{\Delta t} + \mu_a \mathbf{M} \Phi^{\text{fem}} = \mathbf{L}_T.$$

4.7 Diffusion Approximation Equation Discretization

The time-dependent diffusion approximation equation is:

$$\mathbf{M} \frac{\partial \Phi^{\text{fem}}}{c \partial t} + \mathbf{A}_\Phi \Phi^{\text{fem}} = \mathbf{L}_\Phi.$$

Using the finite difference scheme for the time derivative:

$$\frac{\partial \Phi^{\text{fem}}}{c \partial t} \approx \frac{\Phi^{n+1} - \Phi^n}{\Delta t},$$

We then substitute this approximation into the fluence equation to get:

$$\mathbf{M} \frac{\Phi^{n+1} - \Phi^n}{\Delta t} + \mathbf{A}_\Phi \Phi^{\text{fem}} = \mathbf{L}_\Phi.$$

The process to solve this coupled system in a sequential manner is resumed in the algorithm (2).

Algorithm 2 Time-Dependent Heat and Fluence Solver

Require: Δt , T_{final} , material properties, source term S

- 1: Initialize T^0 and Φ^0 from steady-state solutions.
- 2: $N_t \leftarrow T_{\text{final}}/\Delta t$
- 3: Assemble \mathbf{M} , \mathbf{A}_T , \mathbf{A}_Φ , \mathbf{L}_T , and \mathbf{L}_Φ .
- 4: **for** $n = 0$ to $N_t - 1$ **do**
- 5: **Step 1: Solve diffusion approximation equation:**

$$\left(\frac{\mathbf{M}_\Phi}{c\Delta t} + \mathbf{A}_\Phi \right) \Phi^{n+1} = \frac{\mathbf{M}_\Phi}{c\Delta t} \Phi^n + \mathbf{L}_\Phi^{n+1}.$$

- 6: **Step 2: Solve heat equation:**

$$\left(\rho C_p \frac{\mathbf{M}_T}{\Delta t} + \mathbf{A}_T \right) T^{n+1} + \mu_a \mathbf{M}_\Phi \Phi^{n+1} = \rho C_p \frac{\mathbf{M}_T T^n}{\Delta t} + \mathbf{L}_T^{n+1}.$$

- 7: **Step 3: Update right-hand side vectors:**

Update \mathbf{L}_Φ and \mathbf{L}_T with the new values of Φ^{n+1} and T^{n+1} .

- 8: **end for**

Ensure: T^{N_t} and Φ^{N_t}

Note that the coupling is **unidirectional**, meaning that the fluence Φ affects the temperature T , but not vice versa.

5 Simulations

The simulations were performed on the High-Performance Computing (HPC) cluster Gaya. This cluster consists of a DELL PowerEdge R7525 head node and six DELL PowerEdge R6525 compute nodes, providing a total of 768 multi-threaded cores on the compute nodes and 96 cores on the head node. Gaya offers 150 TB of storage for data and an extremely fast 15 TB NVME scratch space. The head node is equipped with two AMD EPYC 7552 48-Core Processors running at 2.2GHz, totaling 192 virtual cores, and 1024 GB of RAM. Each compute node features two AMD EPYC 7713 64-Core Processors running at 2GHz, totaling 256 virtual cores, and 512 GB of RAM. The nodes are interconnected via Broadcom Adv. Dual 10GBASE-T Ethernet and Mellanox ConnectX-6 Dx Dual Port 100 GbE for MPI communication.

In order to keep a good compromise between the parallelization speed up and the cost of MPI communications, the choice of using 12 cores for our simulation was made.

5.1 Eye Geometry

Figure 4 describes an eye geometry with 10 distinct area made with Salome [RBG17] by Thomas Saigre [SPS24; Cha+24].

A 3D tetrahedron mesh (Figure 8) [SPS24] based on this more complex eye geometry was generated using the Salome [CAS22] CAD software utilizing the NETGEN [Sch97] meshing algorithm.

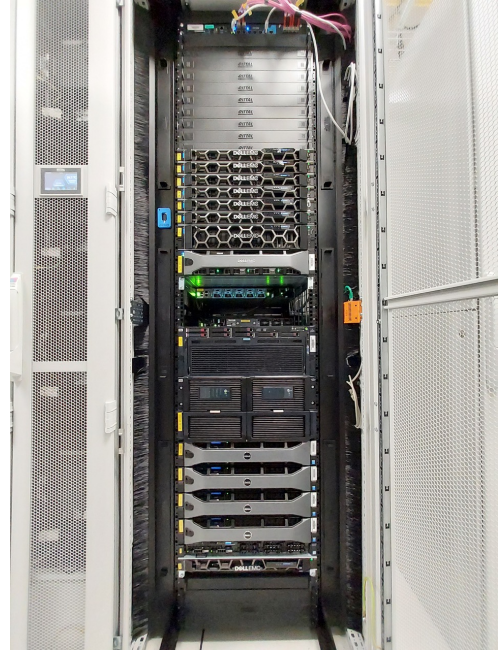
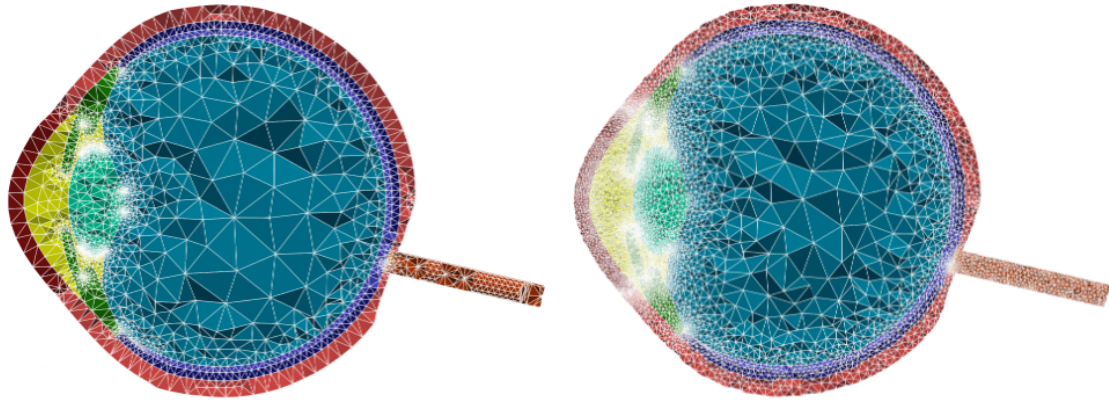


Figure 7: Gaya supercomputer.



(a) Original mesh generated by Salome, with $4.64 \cdot 10^5$ tetrahedrons: $h_{\min} = 5.77 \cdot 10^{-6}$, $h_{\max} = 5.76 \cdot 10^{-3}$. (b) Mesh refined around the anterior and posterior chambers, with $9.4 \cdot 10^5$ elements: $h_{\min} = 5.09 \cdot 10^{-5}$, $h_{\max} = 3.12 \cdot 10^{-3}$.

Figure 8: Meshed geometry of the eye, over a vertical plane. Characteristic sizes are given in meters [SPS24].

As for the FEM basis, in order to be able to solve the problem on the eye geometry with a reasonable computational cost, we choose to use the \mathbb{P}_1 basis functions.

The discretization parameters are summarized in Table 8.

Parameter	Value
Dimension	3
Number of Elements	1,157,768
Number of Edges	1,378,721
Number of Faces	2,327,783
Number of Partitions	12
Number of Points	208,707
h_{average}	4.685408×10^{-4}
h_{\max}	1.140251×10^{-3}
h_{\min}	5.074994×10^{-5}
Order	1
Real Dimension	3
Shape	Simplex _{3,1,3}

Table 8: Discretization parameters

5.2 Solver Settings

The coupling between the heat equation and the fluence equation is implemented using the `coefficient form PDEs` toolbox of the `Feel++` library [Pru+24].

As for the coupling between the RTE-MC and the heat equation, the `heat` toolbox

of the same library is employed [Pru+24]. In the later, the absorption map is represented as a Pdh0 field, *i.e.*, a discontinuous piecewise polynomial of degree 0 (constant value per element). This field is computed within the RTE-MC C++ application and exported as a .h5 file for subsequent use in the heat solver.

The solver utilizes the PETSc [Bal+24] library with the following settings summarized in Table 9.

Component	Settings
Backend	Prefix: <code>heat</code> Type: <code>petsc</code>
KSP (Linear Solver)⁽ⁱ⁾	Absolute Tolerance : 1.0×10^{-50} Divergence Tolerance : 1.0×10^5 Maximum Iterations : 1000 Reuse Preconditioner : 0 Relative Tolerance : 1.0×10^{-8} Solver Type : GMRES
SNES (Nonlinear Solver)⁽ⁱⁱ⁾	Absolute Tolerance : 1.0×10^{-50} Relative Tolerance : 1.0×10^{-8} Step Tolerance : 1.0×10^{-8} Maximum Iterations : 50 Reuse Jacobian : 0
KSP in SNES⁽ⁱⁱⁱ⁾	Maximum Iterations : 1000 Reuse Preconditioner : 0 Relative Tolerance : 1.0×10^{-5}
Preconditioner^(iv)	Type: GAMG

Table 9: Solver settings.

- (i) **KSP (Krylov Subspace Solver)**: Used to solve the linearized systems within the FEM framework. The GMRES method is used here.
- (ii) **SNES (Scalable Nonlinear Equation Solver)**: Solves nonlinear systems using iterative methods. It uses a convergence criterion based on tolerances.
- (iii) **KSP in SNES**: Linear solver applied within each nonlinear iteration of SNES.
- (iv) **Preconditioner**: GAMG (Geometric Algebraic Multigrid) is used to accelerate convergence of the linear solver.

6 Numerical Results

Before presenting the numerical results, we first describe the experimental setup and simulation parameters. To test the RTE-MC heat coupling, we employed a simplified geometry: a cube with dimensions $0.5 \times 0.5 \times 0.25$ centimeters (Figure 9), following the approach of Arnold and Fichera [AF22].

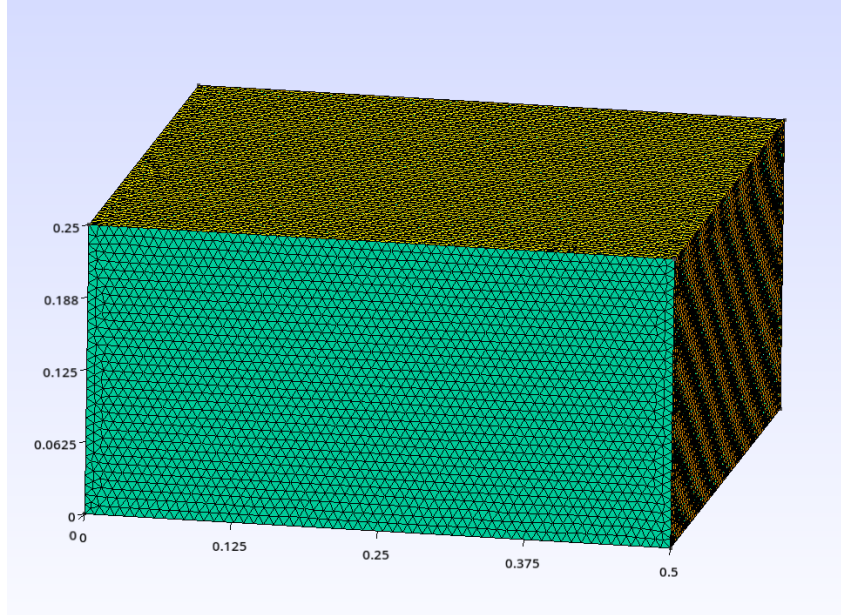


Figure 9: $0.5 \times 0.5 \times 0.25$ cm single layer cube with 81907 nodes and 495013 elements.

The map of absorption was calculated using our RTE-MC code with the parameters summarized in Table 10.

Table 10: Parameters used for the absorption map calculation.

Parameter	Value	Units
Laser impact (x, y, z) coordinates	(0.25, 0.25, 0.25)	cm
Number of photons	2,000,000	—
Beam diameter	0.2	cm
Scattering coefficient (μ_s)	100	cm^{-1}
Absorption coefficient (μ_a)	(1, 2, 3, 4, 5)	cm^{-1}

The Figures 10 and 11 show the resulting absorption map for $\mu_a = 5$ visualized in Log scale with the post processing software Paraview [Kit24].

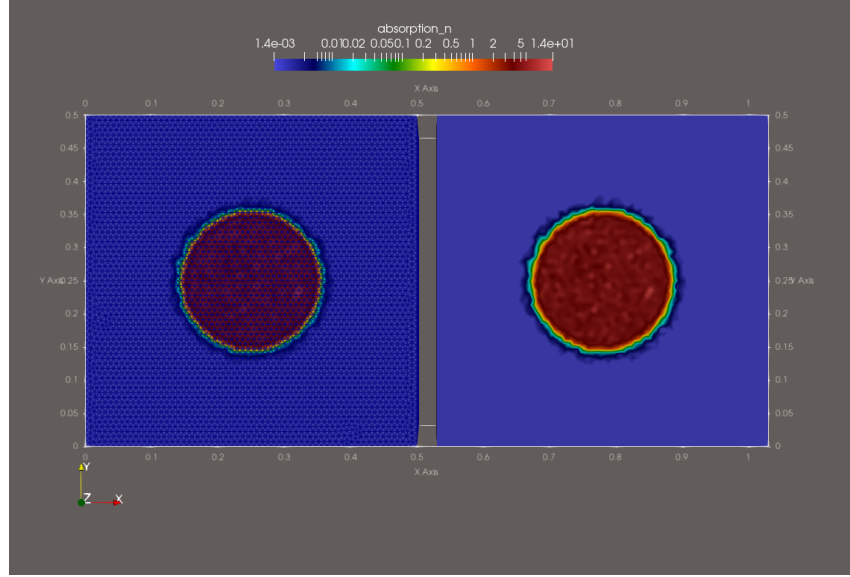


Figure 10: Log scale top view of the absorption map for the cube geometry. On the left shown with the edges.

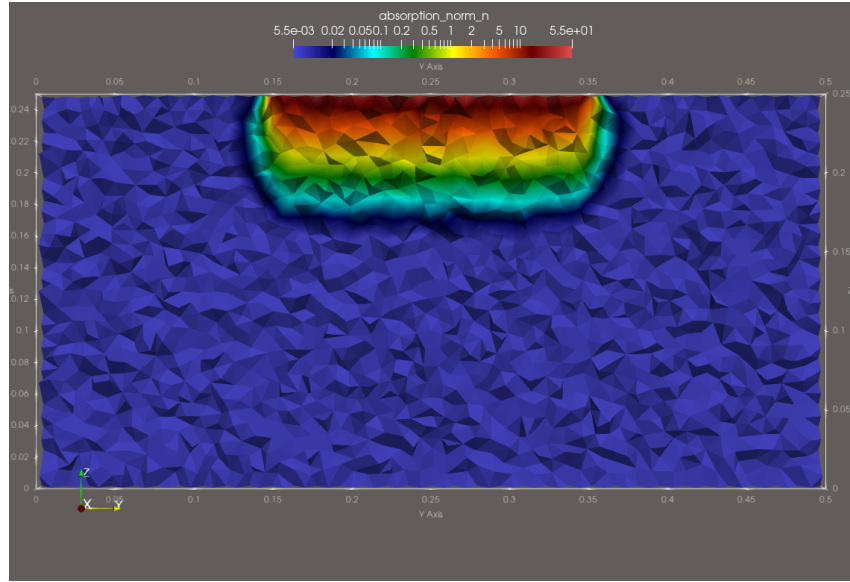


Figure 11: Log scale clipped view of the absorption map for the cube geometry.

The complete absorption map is applied as a source term at each time step. This choice is motivated by the fact that, although the speed of light in the medium is reduced compared to that in vacuum, it remains extremely fast relative to the temporal resolution of the simulation. Specifically, the velocity is given by

$$v_{med} = \frac{c}{n}$$

where

- v_{med} is the velocity of light in the medium,

- c is the speed of light in vacuum,
- n is the refractive index of the medium (*cf.* Table 6).

We import the map of absorption field and use it as a source term in the `heat toolbox` of the Feel++ library [Pru+24]. For this test we choose to use the following homogeneous boundary conditions:

Table 11: Boundary conditions used in the heat equation simulation.

Boundary	Type	Condition
Top face	Neumann	Homogeneous ($\nabla u \cdot n = 0$)
Other faces	Dirichlet	Homogeneous ($u = 0$)

We use a time step of $\Delta t = 0.01$ s and run the simulation for a total time of $T_{\text{final}} = 15$ s. The irradiation time is $T_{\text{irradiation}} = 5$ s. Looking at the imported absorption map (Figure 12), we can notice a strange behavior, the map seems to exhibit unexpected patterns especially on the edges of the irradiation point.

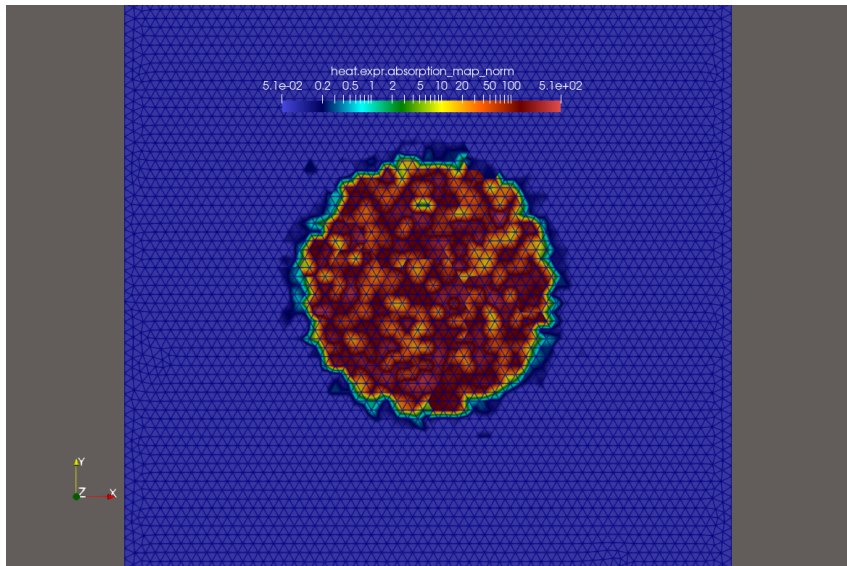
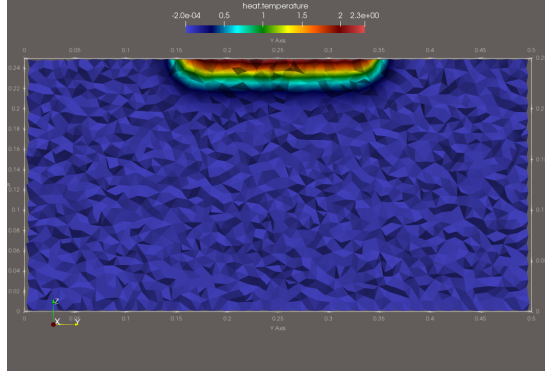
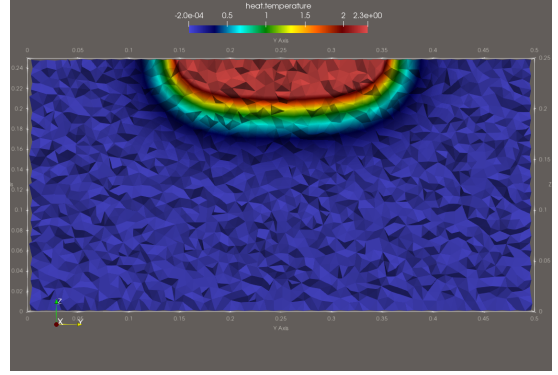


Figure 12: Normalized imported absorption map used by the heat toolbox.

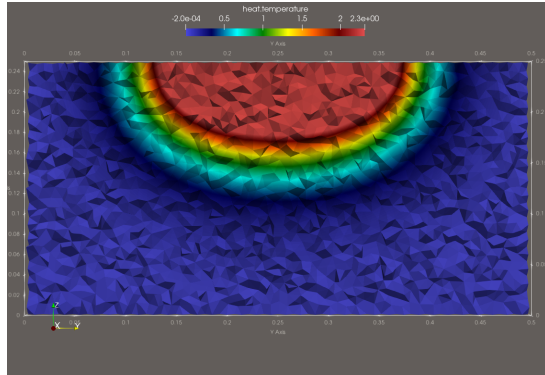
Despite this the coupling seems to work as expected, as shown in Figure 13. Nevertheless, this issue needs to be investigated before making any conclusions. Once the simulation results are thoroughly analyzed, we will be able compare it with experimental data to validate the model.



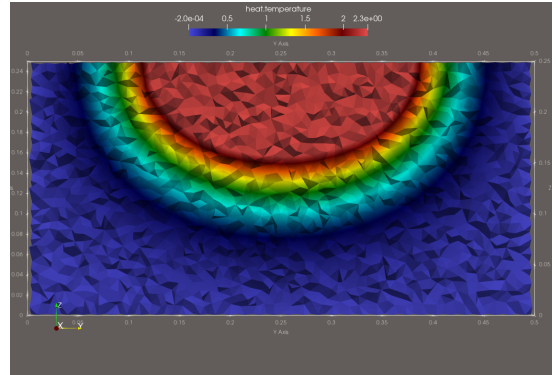
(a) $t = 0.2$ s



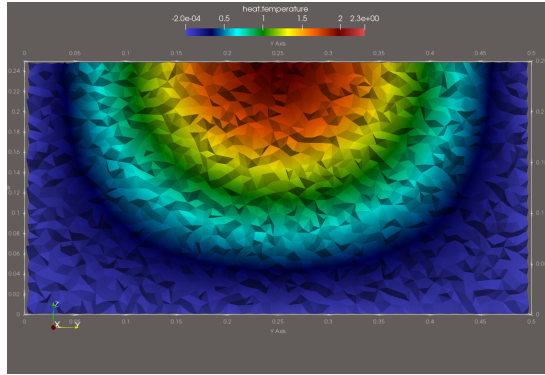
(b) $t = 1.00$ s



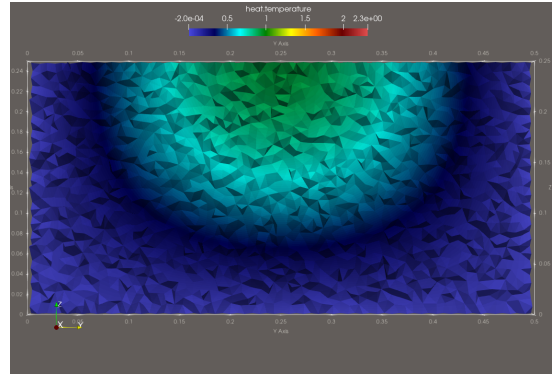
(c) $t = 3.00$ s



(d) $t = 5.00$ s



(e) $t = 10.00$ s



(f) $t = 15.00$ s

Figure 13: Evolution of the temperature distribution on the clipped test cube geometry at different time steps with an irradiation time of $T_{\text{irradiation}} = 5$ s.

7 Toward solving the Inverse Problem

We are interested in solving the inverse problem, *i.e.*, estimating the absorption and scattering coefficients of eye tissues based on the observed temperature distribution. In the context of eye surgery, this temperature distribution can be captured using an infrared camera. To achieve this, we will use an Ensemble Kalman Filter (EnKF) [AF22; Wik24a], designed for parameter estimation.

7.1 Kalman-type Filtering Algorithms

Kalman filtering algorithms provide an efficient, recursive method for estimating the state of a dynamic system from a series of noisy measurements. These algorithms are typically based on the following model:

Evolution Model:

$$x_{j+1} = F(x_j) + \underbrace{\nu_j}_{\text{innovation process}}, \quad (48)$$

where x_j represents the system state at time j , F is a known (possibly non-linear) function, and ν_j represents the innovation process (i.e., the difference between the predicted state and the actual measurement at each time step).

Observation Model:

$$y_{j+1} = G(x_{j+1}) + \underbrace{w_{j+1}}_{\text{observation noise}}, \quad (49)$$

where y_{j+1} is the observation at time $j + 1$, G is a known (possibly non-linear) function, and w_{j+1} denotes the observation noise.

Approximation of the Distribution: The goal is to approximate the probability distribution or posterior distribution of the system's state x_j given the accumulated data D_j up to time j :

$$\pi(x_j|D_j) \rightarrow \pi(x_{j+1}|D_j) \rightarrow \pi(x_{j+1}|D_{j+1}), \quad (50)$$

where D_j represents the data accumulated up to time j :

$$\begin{cases} D_0 = \emptyset, \\ D_{j+1} = D_j \cup \{y_{j+1}\}. \end{cases}$$

The first update in (50) is performed using the *prediction step*, also called the *propagation step*, and the second update is done using the *update step*, which is also known as the *analysis step* or *observation update*.

7.2 Classical Kalman Filter

To understand the Ensemble Kalman Filter (EnKF) [Wik24a], we first need to review the Classical Kalman Filter (KF) [Wik24c]. This filter provides an explicit way of computing the distribution of the state in (50) when the evolution and observation models are linear, and the noise processes are Gaussian. Under these assumptions, the model becomes:

$$\begin{cases} x_{j+1} = Ax_j + \nu_j, \\ y_{j+1} = Px_{j+1} + w_{j+1}, \end{cases} \quad (51)$$

where:

- A is the known state transition matrix,
- P is the known observation matrix,
- $\nu_j \sim \mathcal{N}(0, C)$ is the innovation process,
- $w_{j+1} \sim \mathcal{N}(0, D)$ is the observation noise,
- A and P are assumed to be constant over time.

We further assume that ν_{j+1} is independent of x_j and w_{j+1} is independent of x_{j+1} . The current estimate of the state at time j is denoted $x_{j|j}$, and the prediction of the state at time $j+1$ is denoted $x_{j+1|j}$, obtained by propagating $x_{j|j}$ through the evolution model:

$$x_{j+1|j} = Ax_{j|j} + \nu_{j+1}.$$

Assuming a priori that $x_{j|j} \sim \mathcal{N}(\bar{x}_{j|j}, \Gamma_{j|j})$, the propagation step yields:

$$x_{j+1|j} \sim \mathcal{N}(A\bar{x}_{j|j}, A\Gamma_{j|j}A^T + C).$$

Similarly, the analysis step yields:

$$x_{j+1|j+1} \sim \mathcal{N}(\bar{x}_{j+1|j+1}, \Gamma_{j+1|j+1}),$$

where:

- $\bar{x}_{j|j}$ is the mean of the state estimate at time j ,
- $\bar{x}_{j+1|j+1} = \bar{x}_{j+1|j} + K_{j+1}(y_{j+1} - P\bar{x}_{j+1|j})$,
- $\Gamma_{j+1|j+1} = (I - K_{j+1}P)\Gamma_{j+1|j}$,
- $K_{j+1} = \Gamma_{j+1|j}P^T(P\Gamma_{j+1|j}P^T + D)^{-1}$.

7.3 Ensemble Kalman Filter (EnKF)

The Kalman Filter (KF)[Wik24c] is a powerful tool for estimating the state of a dynamic system from noisy measurements. However, it requires the assumptions of linearity and Gaussian noise, which may not always hold in practice. The Ensemble Kalman Filter (EnKF) is a variant of the KF that relaxes these assumptions and is particularly well-suited for high-dimensional, non-linear systems with non-Gaussian noise.

Instead of maintaining a single estimate of the state, the EnKF maintains an ensemble of state estimates, which are propagated through the evolution model and updated using the observation model. This ensemble approach allows the EnKF to capture the non-linearities and non-Gaussianities present in the system using a Monte Carlo sampling technique.

Propagation Step: Given

$$S_{j|j} = \{x_{j|j}^{(i)}\}_{i=1}^N,$$

the ensemble of N state estimates at time j , we denote

$$\bar{x}_{j|j} = \frac{1}{N} \sum_{i=1}^N x_{j|j}^{(i)} \quad \text{and} \quad \Gamma_{j|j} = \frac{1}{N-1} \sum_{i=1}^N (x_{j|j}^{(i)} - \bar{x}_{j|j})(x_{j|j}^{(i)} - \bar{x}_{j|j})^T,$$

the mean and covariance of the ensemble, respectively.

The non-linear propagation step is performed by applying the evolution model to each ensemble member:

$$x_{j+1|j}^{(i)} = F(x_{j|j}^{(i)}) + \nu_{j+1}^{(i)},$$

where $\nu_{j+1}^{(i)} \sim \mathcal{N}(0, C)$ is the innovation process for the i -th ensemble member.

Analysis Step: Given the observation y_{j+1} , we update the ensemble using the observation model:

$$x_{j+1|j+1}^{(i)} = \operatorname{argmin}_x \left\{ \|y_{j+1}^{(i)} - G(x)\|_D^2 + \|x - x_{j+1|j}^{(i)}\|_{\Gamma_{j+1|j}^2} \right\},$$

where $\|u\|_D^2 = u^T D^{-1} u$ is the Mahalanobis distance (which measures the distance between a point and a distribution) with respect to the observation noise covariance matrix D (symmetric positive-definite).

8 Conclusion

The study of heat-fluence coupling in ocular tissues, as presented in this project, underscores the intricate interplay of mathematical modeling, numerical simulation, and physical parameter estimation. Despite significant progress in capturing the dynamic of this coupling, the complexity of the underlying physics, coupled with the variability of eye tissue properties and laser settings, posed substantial challenges. The preliminary simulations performed on the simplified cube geometry demonstrate that the RTE-MC and heat equation coupling is functional and can reproduce expected temperature evolutions. However, anomalies in the imported absorption map, particularly near the edges of the irradiation point, indicate that further investigation and validation are required before applying the method to more realistic eye geometries. Future work will focus on refining the absorption map generation, extending the simulations to anatomically accurate eye models, and performing a systematic comparison with experimental data. Additionally, sensitivity analyses on tissue optical and thermal parameters will help quantify uncertainties and improve the robustness of the model.

Overall, this study establishes a solid foundation for modeling laser-tissue interactions in ophthalmology, providing insights into temperature dynamics and paving the way for more precise and patient-specific simulations in the future.

9 Prospects

The study of the heat-eye interactions is vast and complex, and there are many avenues for further research. Here are some prospects we identify for future work:

1. **Improve Eye Geometry:** Our current geometry is quite complex but could nonetheless be improved. For example, in the case of our application, we could improve it by adding a system of layer in order to be able to use different absorption and scattering coefficients according to the tissue's depth as well as a RPE layer.
2. **RTE-MC improvement:** Continue enhance the RTE-MC code to improve its accuracy and efficiency. Especially the handling of complex tissue geometries and their interfaces.
3. **Mesh convergence:** Investigate the mesh convergence of our model by extracting values at different points of interest and comparing them while refining the mesh to assess if the results converge to a certain value.
4. **Model comparison validation:** Validate our model by taking more time to compare it with other models and experimental data.
5. **Sensitivity analysis:** Conduct sensitivity analyses to identify the most influential parameters affecting the model's predictions and to better understand the system's behavior.
6. **ROMs:** Investigate the use of **Reduced Order Models** to speed up the simulation process.
7. **Inverse problem:** Explore the possibility of solving an inverse problem to estimate the tissue's optical and thermal properties based on experimental data via the use of data assimilation techniques such as the Ensemble Kalman Filter (EnKF). Alternatively, explore the use of machine learning techniques to infer these properties from the data.

Appendix A: Approximation Error Metrics for Schlick vs. Fresnel

To evaluate the accuracy of the generalized Schlick approximation, we computed error metrics against the Fresnel equations across all tissue interfaces of the eye model. Sampling was performed over 90 angles in $[0^\circ, 90^\circ]$. The refractive indices used for the calculations are for a 577 nm wavelength and are summarized in Table 6.

The TIR acronym reffers to the **Total Internal Reflection** angle, it occurs when light travels from a medium with a higher refractive index to a medium with a lower refractive index, and the angle of incidence exceeds a certain critical angle. Beyond this angle, refraction becomes impossible, and all the incident light is reflected back into the first medium. Mathematically, TIR happens when $\sin \theta_t > 1$, which has no physical solution for θ_t , indicating that transmission does not occur. In the context of our study, TIR arises in transitions such as from the vitreous humour to the lens or from the cornea to the air, where $n_1 > n_2$. The Fresnel equations handle this condition naturally, setting the reflectance $R = 1$ in such cases. However, approximations like the Schlick model must account for TIR explicitly to remain accurate. The generalized Schlick approximation incorporates this by detecting when $\sin \theta_t > 1$ and setting $R = 1$ accordingly, ensuring that the reflectance curve remains physically plausible even beyond the critical angle.

Table 12: Per-interface reflectance error between generalized Schlick and Fresnel reflectance.

Interface	n_1	n_2	MAE (all)	MAE (< TIR)	Max Error	Angle at Max (°)
Air → Cornea	1.000	1.375	0.009 71	0.009 71	0.050 20	84.1
Cornea → Air	1.375	1.000	0.002 61	0.005 05	0.050 20	46.3
Cornea → Aq. Humour	1.375	1.335	0.015 85	0.024 63	0.110 62	86.1
Aq. Humour → Cornea	1.335	1.375	0.012 08	0.012 08	0.076 26	84.0
Aq. Humour → Lens Grad A	1.335	1.367	0.072 13	0.072 13	0.518 13	86.2
Lens Grad A → Aq. Humour	1.367	1.335	0.073 51	0.108 88	0.518 13	86.2
Lens Grad A → Lens Grad B	1.367	1.385	0.065 92	0.065 92	0.466 90	86.3
Lens Grad B → Lens Grad A	1.385	1.367	0.064 86	0.093 63	0.466 90	86.3
Lens Grad B → Vitreous	1.385	1.336	0.034 86	0.048 78	0.279 38	86.2
Vitreous → Lens Grad B	1.336	1.385	0.035 76	0.035 76	0.231 10	85.9
Vitreous → Retina	1.336	1.358	0.078 22	0.078 22	0.544 34	86.2
Retina → Vitreous	1.358	1.336	0.077 41	0.113 09	0.544 34	86.2
Retina → Choroid	1.358	1.356	0.081 98	0.081 98	0.569 27	86.3
Choroid → Retina	1.356	1.358	0.082 11	0.082 11	0.569 27	86.3
Choroid → Sclera	1.356	1.366	0.08776	0.08776	0.58769	86.3
Sclera → Choroid	1.366	1.356	0.087 17	0.126 27	0.587 69	86.3

Summary:

- **Average MAE (all):** 0.0443
- **Max MAE:** 0.0878 (Choroid → Sclera)
- **Max absolute error:** 0.5877 at 86.3°

These results confirm that the generalized Schlick approximation yields reasonable accuracy across biologically relevant interfaces in the human eye model, with increasing error primarily at high incidence angles near total internal reflection.

A References

References

- [21] “The Schlick Fresnel Approximation”. In: Zander Majercik. *Ray Tracing Gems II*. Berkeley, CA: Apress, 2021, pp. 109–114. ISBN: 978-1-4842-7184-1 978-1-4842-7185-8. DOI: [10.1007/978-1-4842-7185-8_9](https://doi.org/10.1007/978-1-4842-7185-8_9). URL: https://link.springer.com/10.1007/978-1-4842-7185-8_9 (visited on 07/25/2025).
- [ACS14] Andrea Arnold, Daniela Calvetti, and Erkki Somersalo. “Parameter Estimation for Stiff Deterministic Dynamical Systems via Ensemble Kalman Filter”. In: *Inverse Problems* 30.10 (Oct. 1, 2014), p. 105008. ISSN: 0266-5611, 1361-6420. DOI: [10.1088/0266-5611/30/10/105008](https://doi.org/10.1088/0266-5611/30/10/105008). URL: <https://iopscience.iop.org/article/10.1088/0266-5611/30/10/105008> (visited on 10/17/2024).
- [AEH15] Amin Joukar, Erfan Nammakie, and Hanieh Niroomand-Oscuii. “A Comparative Study of Thermal Effects of 3 Types of Laser in Eye: 3D Simulation with Bioheat Equation”. In: *Journal of Thermal Biology* (2015).
- [AF22] Andrea Arnold and Loris Fichera. “Identification of Tissue Optical Properties during Thermal Laser-tissue Interactions: An Ensemble Kalman Filter-Based Approach”. In: *International Journal for Numerical Methods in Biomedical Engineering* 38.4 (Apr. 2022), e3574. ISSN: 2040-7939, 2040-7947. DOI: [10.1002/cnm.3574](https://doi.org/10.1002/cnm.3574). URL: <https://onlinelibrary.wiley.com/doi/10.1002/cnm.3574>.
- [Afl+20a] Kobi Aflalo et al. “Theoretical Investigation of Using a Yellow (577nm) Laser for Diabetic Retinopathy”. In: *OSA Continuum* 3.11 (Nov. 15, 2020), pp. 3253–3266. ISSN: 2578-7519. DOI: [10.1364/OSAC.399120](https://doi.org/10.1364/OSAC.399120). URL: <https://opg.optica.org/osac/abstract.cfm?uri=osac-3-11-3253> (visited on 02/17/2025).
- [Afl+20b] Kobi Aflalo et al. “Theoretical Investigation of Using a Yellow (577nm) Laser for Diabetic Retinopathy”. In: *OSA Continuum* 3.11 (Nov. 15, 2020), pp. 3253–3266. ISSN: 2578-7519. DOI: [10.1364/OSAC.399120](https://doi.org/10.1364/OSAC.399120). URL: <https://opg.optica.org/osac/abstract.cfm?uri=osac-3-11-3253> (visited on 07/21/2025).
- [Bal+24] Satish Balay et al. *PETSc Web Page*. 2024. URL: <https://petsc.org/>.
- [Blo19] FindLight Blog. *Laser Tissue Interactions: Biological Factors to Consider for Dermatology*. 2019. URL: <https://www.findlight.net/blog/laser-tissue-interactions/>.
- [CAS22] Open CASCADE. *SALOME: The Open Source Integration Platform for Numerical Simulation*. 2022. URL: <https://salome-project.org>.
- [Cha+24] Vincent Chabannes et al. *A 3D Geometrical Model and Meshing Procedures for the Human Eyeball*. Version v1.0.0-preview.2. Zenodo, Sept. 23, 2024. DOI: [10.5281/ZENODO.13829740](https://doi.org/10.5281/ZENODO.13829740). URL: <https://zenodo.org/doi/10.5281/zenodo.13829740>.

- [Chr+24] Christophe Prud'homme et al. *Feelpp/Feelpp: Feel++ Release V111 Preview.9*. Version v0.111.0-preview.9. Zenodo, Mar. 2024. DOI: [10.5281/zenodo.10837178](https://doi.org/10.5281/zenodo.10837178). URL: <https://doi.org/10.5281/zenodo.10837178>.
- [CPP08] Mario Cvetkovic, Dragan Poljak, and Andres Peratta. “Thermal Modelling of the Human Eye Exposed to Laser Radiation”. In: *2008 16th International Conference on Software, Telecommunications and Computer Networks*. 2008 16th International Conference on Software, Telecommunications and Computer Networks. Sept. 2008, pp. 16–20. DOI: [10.1109/SOFTCOM.2008.4669444](https://ieeexplore.ieee.org/document/4669444). URL: <https://ieeexplore.ieee.org/document/4669444?arnumber=4669444> (visited on 02/17/2025).
- [Enp93] Enping Chen. “Refractive Indices of the Rat Retinal Layers”. In: *Ophthalmic Res* (1993), p. 4. DOI: [10.1159/000267223](https://doi.org/10.1159/000267223).
- [Eye21] EyeWiki. “Lasers in Ophthalmic Surgery”. In: *EyeWiki* (2021). URL: https://eyewiki.org/Lasers_%28surgery%29.
- [GR24] Christophe Geuzaine and Jean-François Remacle. *Gmsh*. 2024. URL: <http://gmsh.info/>.
- [Heu+14] Nico Heussner et al. “Prediction of Temperature and Damage in an Irradiated Human Eye—Utilization of a Detailed Computer Model Which Includes a Vectorial Blood Stream in the Choroid”. In: *Computers in Biology and Medicine* (2014), p. 9.
- [HG41] L. G. Henyey and J. L. Greenstein. “Diffuse Radiation in the Galaxy”. In: *The Astrophysical Journal* 93 (1941), pp. 70–83.
- [J J82] J J W Lagendijk. “A Mathematical Model to Calculate Temperature Distributions in Human and Rabbit Eyes during Hyperthermic Treatment”. In: *Physics in Medicine & Biology* 27.11 (Nov. 1, 1982), pp. 1301–1311. ISSN: 0031-9155, 1361-6560. DOI: [10.1088/0031-9155/27/11/001](https://doi.org/10.1088/0031-9155/27/11/001). URL: <https://iopscience.iop.org/article/10.1088/0031-9155/27/11/001> (visited on 08/20/2025).
- [Kit24] Kitware. *ParaView*. 2024. URL: <https://www.paraview.org/>.
- [Kle+21] Viktoria Kleyman et al. *State and Parameter Estimation for Model-Based Retinal Laser Treatment*. Mar. 4, 2021. DOI: [10.48550/arXiv.2103.03189](https://arxiv.org/abs/2103.03189). arXiv: [2103.03189 \[eess\]](https://arxiv.org/abs/2103.03189). URL: [http://arxiv.org/abs/2103.03189](https://arxiv.org/abs/2103.03189) (visited on 08/20/2025). Pre-published.
- [Kra+75] Piro O. Kramar et al. “THE OCULAR EFFECTS OF MICROWAVES ON HYPOTHERMIC RABBITS: A STUDY OF MICROWAVE CATARACTOGENIC MECHANISMS*”. In: *Annals of the New York Academy of Sciences* 247.1 (Feb. 1975), pp. 155–165. ISSN: 0077-8923, 1749-6632. DOI: [10.1111/j.1749-6632.1975.tb35992.x](https://doi.org/10.1111/j.1749-6632.1975.tb35992.x). URL: <https://nyaspubs.onlinelibrary.wiley.com/doi/10.1111/j.1749-6632.1975.tb35992.x> (visited on 08/20/2025).
- [LB97] Hwey-Lan Liou and Noel A. Brennan. “Anatomically Accurate, Finite Model Eye for Optical Modeling”. In: *JOSA A* 14.8 (Aug. 1, 1997), pp. 1684–1695. ISSN: 1520-8532. DOI: [10.1364/JOSAA.14.001684](https://doi.org/10.1364/JOSAA.14.001684). URL: <https://opg.optica.org/josaa/abstract.cfm?uri=josaa-14-8-1684> (visited on 07/23/2025).

- [Med22] Weill Cornell Medicine. “Corneal and Anterior Segment Diseases”. In: *Weill Cornell Medicine* (2022). URL: <https://weillcornell.org/corneal-and-anterior-segment-diseases>.
- [Mir+21] Héctor Miras Del Río et al. “A Monte Carlo Dose Calculation System for Ophthalmic Brachytherapy Based on a Realistic Eye Model”. In: *Medical Physics* 48.8 (Aug. 2021), pp. 4542–4559. ISSN: 2473-4209. DOI: [10.1002/mp.15045](https://doi.org/10.1002/mp.15045). PMID: [34250607](#).
- [MRA13] Seyyed Abbas Mirnezami, Mahdi Rajaei Jafarabadi, and Maryam Abrishami. “Temperature Distribution Simulation of the Human Eye Exposed to Laser Radiation”. In: *Journal of Lasers in Medical Sciences* 4.4 (2013), pp. 175–181. ISSN: 2008-9783. PMID: [25606327](#). URL: <https://www.ncbi.nlm.nih.gov/pmc/articles/PMC4282006/> (visited on 02/07/2025).
- [Nar17] Arunn Narasimhan. “Heat and Mass Transfer Processes in the Eye”. In: *Handbook of Thermal Science and Engineering*. Ed. by Francis A. Kulacki. Cham: Springer International Publishing, 2017, pp. 1–35. ISBN: 978-3-319-32003-8. DOI: [10.1007/978-3-319-32003-8_72-2](https://doi.org/10.1007/978-3-319-32003-8_72-2). URL: http://link.springer.com/10.1007/978-3-319-32003-8_72-2.
- [NJ12] Arunn Narasimhan and Kaushal Kumar Jha. “Bio-Heat Transfer Simulation of Retinal Laser Irradiation”. In: *International Journal for Numerical Methods in Biomedical Engineering* 28.5 (2012), pp. 547–559. ISSN: 2040-7947. DOI: [10.1002/cnm.1489](https://doi.org/10.1002/cnm.1489). URL: <https://onlinelibrary.wiley.com/doi/abs/10.1002/cnm.1489> (visited on 02/05/2025).
- [NOR08] Eddie-Yin-Kwee Ng, Ean-Hin Ooi, and U. Rajendra Archarya. “A Comparative Study between the Two-Dimensional and Three-Dimensional Human Eye Models”. In: *Mathematical and Computer Modelling* 48.5 (Sept. 1, 2008), pp. 712–720. ISSN: 0895-7177. DOI: [10.1016/j.mcm.2007.11.011](https://doi.org/10.1016/j.mcm.2007.11.011). URL: <https://www.sciencedirect.com/science/article/pii/S0895717707003548> (visited on 08/20/2025).
- [Nor22] Norlase. “Retinal Holes and Laser Treatment”. In: *Norlase* (2022). URL: <https://norlase.com/retinal-holes/>.
- [NRW96] Babak Nemati, H. Grady Rylander, and Ashley J. Welch. “Optical Properties of Conjunctiva, Sclera, and the Ciliary Body and Their Consequences for Transscleral Cyclophotocoagulation”. In: *Applied Optics* 35.19 (July 1, 1996), pp. 3321–3327. ISSN: 2155-3165. DOI: [10.1364/AO.35.003321](https://doi.org/10.1364/AO.35.003321). URL: <https://opg.optica.org/ao/abstract.cfm?uri=ao-35-19-3321> (visited on 07/23/2025).
- [Oph21] American Academy of Ophthalmology. “Thermal Laser and PDT for AMD-Related Diseases”. In: *AAO* (2021). URL: <https://www.aao.org/munnerlyn-laser-surgery-center/thermal-laser-pdt-amd-related-diseases>.
- [Oph23] American Academy of Ophthalmology. “LASIK, SMILE, PRK”. In: *AAO Eye Health* (2023). URL: <https://www.aao.org/eye-health/treatments/new-eyehealthcontent-4>.

- [Paj+21] Bojan Pajic et al. “Why Use Ultrashort Pulses in Ophthalmology and Which Factors Affect Cut Quality”. In: *Medicina* 57.7 (July 8, 2021), p. 700. ISSN: 1010-660X. DOI: [10.3390/medicina57070700](https://doi.org/10.3390/medicina57070700). PMID: 34356980. URL: <https://www.ncbi.nlm.nih.gov/pmc/articles/PMC8304458/> (visited on 02/03/2025).
- [Pru+24] Christophe Prud’homme et al. *Feelpp/Feelpp: Feel++ Release V111 Preview.10*. Version v0.111.0-preview.10. Zenodo, July 15, 2024. DOI: [10.5281/zenodo.12742155](https://doi.org/10.5281/zenodo.12742155). URL: <https://zenodo.org/doi/10.5281/zenodo.12742155>.
- [Pub14] PubMed. “Femtosecond laser-assisted cataract surgery”. In: *National Library of Medicine* (2014). URL: <https://pubmed.ncbi.nlm.nih.gov/24699157/>.
- [RBG17] Alejandro Ribes, Adrien Bruneton, and Anthony Geay. *SALOME: An Open-Source Simulation Platform Integrating ParaView*. 2017. DOI: [10.13140/RG.2.2.12107.08485](https://doi.org/10.13140/RG.2.2.12107.08485). URL: <http://rgdoi.net/10.13140/RG.2.2.12107.08485>. Pre-published.
- [Reg+19] Simon Regal et al. “Determination of Optical Parameters of the Porcine Eye and Development of a Simulated Model”. In: *Journal of Biophotonics* 12.11 (2019), e201800398. ISSN: 1864-0648. DOI: [10.1002/jbio.201800398](https://doi.org/10.1002/jbio.201800398). URL: <https://onlinelibrary.wiley.com/doi/abs/10.1002/jbio.201800398> (visited on 07/21/2025).
- [RS18] Sahar Rahbar and Mehrdad Shokoh-Saremi. “Mathematical Modeling of Laser Linear Thermal Effects on the Anterior Layer of the Human Eye”. In: *Optics & Laser Technology* 99 (Feb. 1, 2018), pp. 72–80. ISSN: 0030-3992. DOI: [10.1016/j.optlastec.2017.09.033](https://doi.org/10.1016/j.optlastec.2017.09.033). URL: <https://www.sciencedirect.com/science/article/pii/S0030399217303377> (visited on 02/04/2025).
- [S R99] S R Arridge. “Optical Tomography in Medical Imaging”. In: *IOP* 15 (1999), p. 54. DOI: [10.1088/0266-5611/15/2/022](https://doi.org/10.1088/0266-5611/15/2/022).
- [Sai24] Thomas Saigre. “Mathematical Modeling, Simulation and Reduced Order Modeling of Ocular Flows and Their Interactions: Building the Eye’s Digital Twin”. Theses. Université de Strasbourg, Dec. 2024. URL: <https://theses.hal.science/tel-04813671>.
- [SB03] S K Sharma and Srilekha Banerjee. “Role of Approximate Phase Functions in Monte Carlo Simulation of Light Propagation in Tissues”. In: *Journal of Optics A: Pure and Applied Optics* 5.3 (May 1, 2003), pp. 294–302. ISSN: 1464-4258. DOI: [10.1088/1464-4258/5/3/324](https://doi.org/10.1088/1464-4258/5/3/324). URL: <https://iopscience.iop.org/article/10.1088/1464-4258/5/3/324> (visited on 08/18/2025).
- [Sch97] Joachim Schöberl. “NETGEN An Advancing Front 2D/3D-mesh Generator Based on Abstract Rules”. In: *Computing and Visualization in Science* 1.1 (July 1, 1997), pp. 41–52. ISSN: 1432-9360, 1433-0369. DOI: [10.1007/s007910050004](https://doi.org/10.1007/s007910050004). URL: <http://link.springer.com/10.1007/s007910050004>.
- [Sco88a] J A Scott. “A Finite Element Model of Heat Transport in the Human Eye”. In: *Physics in Medicine and Biology* 33.2 (Feb. 1, 1988), pp. 227–242. ISSN: 0031-9155, 1361-6560. DOI: [10.1088/0031-9155/33/2/003](https://doi.org/10.1088/0031-9155/33/2/003). URL: <https://iopscience.iop.org/article/10.1088/0031-9155/33/2/003> (visited on 08/20/2025).

- [Sco88b] J A Scott. “A Finite Element Model of Heat Transport in the Human Eye”. In: *Physics in Medicine and Biology* 33.2 (Feb. 1, 1988), pp. 227–242. ISSN: 0031-9155, 1361-6560. DOI: [10.1088/0031-9155/33/2/003](https://doi.org/10.1088/0031-9155/33/2/003). URL: <https://iopscience.iop.org/article/10.1088/0031-9155/33/2/003>.
- [Sem17] Vladimir Semenyuk. “Thermal Interaction of Multi-Pulse Laser Beam with Eye Tissue during Retinal Photocoagulation: Analytical Approach”. In: *International Journal of Heat and Mass Transfer* 112 (Sept. 2017), pp. 480–488. ISSN: 00179310. DOI: [10.1016/j.ijheatmasstransfer.2017.05.013](https://doi.org/10.1016/j.ijheatmasstransfer.2017.05.013). URL: <https://linkinghub.elsevier.com/retrieve/pii/S001793101730933X> (visited on 02/17/2025).
- [SLG06] Krish D. Singh, Nicola S. Logan, and Bernard Gilmartin. “Three-Dimensional Modeling of the Human Eye Based on Magnetic Resonance Imaging”. In: *Investigative Ophthalmology & Visual Science* 47.6 (June 1, 2006), p. 2272. ISSN: 1552-5783. DOI: [10.1167/iovs.05-0856](https://doi.org/10.1167/iovs.05-0856). URL: <http://iovs.arvojournals.org/article.aspx?doi=10.1167/iovs.05-0856>.
- [SPS24] Thomas Saigre, Christophe Prud’homme, and Marcela Szopos. “Model Order Reduction and Sensitivity Analysis for Complex Heat Transfer Simulations inside the Human Eyeball”. In: *International Journal for Numerical Methods in Biomedical Engineering* 40.11 (Sept. 9, 2024), e3864. ISSN: 2040-7939, 2040-7947. DOI: [10.1002/cnm.3864](https://doi.org/10.1002/cnm.3864). URL: <https://onlinelibrary.wiley.com/doi/10.1002/cnm.3864>.
- [Tim22] Optometry Times. “New Data in Anterior Segment Laser Surgery”. In: *Optometry Times* (2022). URL: <https://www.optometrytimes.com/view/new-data-in-anterior-segment-laser-surgery>.
- [TLW22] Linh T D Truong, Peter J Lesniewski, and A Bruce Wedding. “Heat Transfer Simulation in Laser Irradiated Retinal Tissues”. In: *Biomedical Physics & Engineering Express* 8.1 (Jan. 1, 2022), p. 015027. ISSN: 2057-1976. DOI: [10.1088/2057-1976/ac3f51](https://doi.org/10.1088/2057-1976/ac3f51). URL: <https://iopscience.iop.org/article/10.1088/2057-1976/ac3f51> (visited on 02/19/2025).
- [Tod17] Retina Today. “Laser Therapy for Diabetic Retinopathy and Diabetic Macular Edema”. In: *Retina Today* (2017). URL: <https://retinatoday.com/articles/2017-may-june/laser-therapy-for-diabetic-retinopathy-and-diabetic-macular-edema>.
- [Wik24a] Wikipedia. *Ensemble Kalman filter*. 2024. URL: https://en.wikipedia.org/wiki/Ensemble_Kalman_filter.
- [Wik24b] Wikipedia. *Finite Element Method*. 2024. URL: https://en.wikipedia.org/wiki/Finite_element_method.
- [Wik24c] Wikipedia. “Kalman Filter”. In: *Wikipedia* (2024). URL: https://en.wikipedia.org/wiki/Kalman_filter.
- [WT79] Walter Egan and Theodore W. Hilgeman. *Optical Properties of Inhomogeneous Materials*. 1979.

- [WV10] Ashley J. Welch and Martin J.C. Van Gemert. “Overview of Optical and Thermal Laser-Tissue Interaction and Nomenclature”. In: *Optical-Thermal Response of Laser-Irradiated Tissue*. Ed. by Ashley J. Welch and Martin J.C. Van Gemert. Dordrecht: Springer Netherlands, 2010, pp. 3–11. ISBN: 978-90-481-8830-7 978-90-481-8831-4. DOI: [10.1007/978-90-481-8831-4_1](https://doi.org/10.1007/978-90-481-8831-4_1). URL: https://link.springer.com/10.1007/978-90-481-8831-4_1 (visited on 12/07/2024).
- [Zan+25] G. Zanellati et al. “A Review of Optical and Thermal Eye Tissue Parameters for Improved Computational Models in Retinal Laser Therapy”. In: *Progress in Biomedical Engineering (Bristol, England)* 7.1 (Jan. 7, 2025). ISSN: 2516-1091. DOI: [10.1088/2516-1091/ad9aec](https://doi.org/10.1088/2516-1091/ad9aec). PMID: [39773849](#).
- [Zha+23] P. H. Zhao et al. “A Coupled BioHeat Transfer Model for Customized Whole-Eye Modeling in Retinal Laser Surgery”. In: *International Journal of Thermal Sciences* 183 (Jan. 1, 2023), p. 107897. ISSN: 1290-0729. DOI: [10.1016/j.ijthermalsci.2022.107897](https://doi.org/10.1016/j.ijthermalsci.2022.107897). URL: <https://www.sciencedirect.com/science/article/pii/S1290072922004252> (visited on 02/05/2025).